Authors
Werner Badenhorst (ORCID: 0000-0003-2387-1100)
Tania Hanekom (ORCID: 0000-0003-2455-7332)
Johan J. Hanekom (ORCID: 0000-0003-4025-5019)

Title
Analysis of a purely conductance-based stochastic nerve fibre model as applied to compound models of populations of human auditory nerve fibres used in cochlear implant simulations

Affiliation and address of authors
Department of Electrical, Electronic and Computer Engineering,
University of Pretoria, Lynnwood Road
Pretoria 0002, South Africa

Corresponding author details
e-mail: werner.badenhorst@up.ac.za
Tel: +27 12 420 2587
Fax: +27 12 362 5000

Abstract
The study presents the application of a purely conductance-based stochastic nerve fibre model to human auditory nerve fibres within finite element volume conduction models of a semi-generic head and user-specific cochleae. The stochastic, threshold and temporal characteristics of the human model are compared and successfully validated against physiological feline results with the application of a mono-polar, bi-phasic, cathodic first stimulus. Stochastic characteristics validated include: (i) the log(*Relative Spread*) vs log(*fibre diameter*) distribution for the discharge probability vs stimulus intensity plots and (ii) the required exponential membrane noise versus transmembrane voltage distribution. Intra-user, and to a lesser degree inter-user, comparisons are made with respect to threshold and dynamic range at short and long pulse widths for full vs degenerate single fibres as well as for populations of degenerate fibres of a single user having distributed and aligned somas with varying and equal diameters. Temporal characteristics validated through application of different stimulus pulse rates and different stimulus intensities include: (i) discharge rate, latency and latency standard deviation vs stimulus intensity, (ii) period histograms and (iii) inter-spike-interval histograms. Although the stochastic population model does not reduce the modelled single deterministic fibre threshold, the simulated stochastic and temporal characteristics show that it could be used in future studies to model user-specific temporally encoded information, which influences the speech perception of CI users.

Keywords
Cochlear implant
Compound auditory nerve fibre model
Conductance based
Stochastic nerve fibre model
Temporal characteristics
Population nerve fibre model
Volume conduction model

1. Introduction

A cochlear implant (CI) directly stimulates the surviving and functioning auditory nerve fibres (ANFs) with electrical pulses via an array of electrodes implanted inside the cochlea to provide profoundly deaf persons with a measure of sound perception and, in particular, speech perception (Smit et al. 2009). Improving the sound perception of the CI user requires an improvement in stimulation strategies (Arora et al. 2009; Fu and Shannon 2000; Galvin and Fu 2005; Middlebrooks 2004) and CI electrode designs (Briaire and Frijns 2006; Kreft et al. 2004; Kwon and Van Den Honert 2006; Snel-Bongers et al. 2012). Improved stimulation strategies and electrode designs may in turn benefit from a better understanding of:

i. the auditory nerve properties through neural modelling (Badenhorst et al. 2016; Bruce et al. 1999b; Hanekom and Hanekom 2016; Macherey et al. 2007; Rattay et al. 2001a; Rattay et al. 2001b; Smit et al. 2010; van Gendt et al. 2016),
ii. the wide variance in performance and perceptual experience produced by the CI among CI users (Ferguson et al. 2003; Firszt et al. 2004; Nadol Jr 1997; Skinner 2003), and
iii. the effect of various stimulation strategies and electrode designs through computational modelling (Kalkman et al. 2016).

To better understand and hence predict the electrically stimulated neural response (ESNR) caused by the activation of an electrode, numerous ANF models (Frijns et al. 1994; Imennov and Rubinstein 2009; O'Brien and Rubinstein 2016; Rattay 1990; Rattay et al. 2001b; Smit et al. 2010) and volume conduction (VC) models (Frijns et al. 1995; Hanekom 2001; Kalkman et al. 2014; Malherbe et al. 2015; Rattay et al. 2001a) have been developed since the revolutionary nerve fibre model by Hodgkin and Huxley (1952) (HH). The temporally encoded information contained in a CI's ESNR (Cartee et al. 2000; Sachs et al. 1983; van den Honert and Stypulkowski 1987) influences speech perception of CI users (Fu and Shannon 2000; Galvin and Fu 2005; Vandali et al. 2000), as well as pitch perception of complex tones and pure-tone frequency discrimination (Javel 1990). The temporally encoded information within the ESNR is in turn affected by the high frequency pulsatile stimulation of CI speech processors (Javel and Shepherd 2000; van den Honert and Stypulkowski 1987). In addition to estimating the neural excitation threshold (the stimulus intensity at which the neuron is excited to provide a propagating action potential (AP)), the desired models should therefore also model the ANF temporal characteristics (Bruce et al. 1999b; Cartee et al. 2000; Rattay et al. 2001b). This is generally done through the use of discharge rate and latency vs stimulus intensity plots as well as period and inter-spike interval (ISI) histograms, as is generally done in physiological experiments (Javel 1990; Javel and Shepherd 2000; Javel et al. 1987; Shepherd and Javel 1997; Shepherd and Javel 1999).

One of the important properties of a nerve fibre that impacts its temporal characteristics is variance in threshold stimulus intensity (Hales et al. 2004; Javel et al. 1987; Verveen 1962; Verveen and Derksen 1968). This threshold variance has been shown to be primarily caused by the stochastic behaviour or microscopic fluctuations of the node of Ranvier's voltage dependent sodium channels (Hales et al. 2004; Rubinstein 1995; Sigworth 1980) of which the intensity is a function of the membrane voltage (Verveen and Derksen 1968). A number of methods are followed to model the threshold variability in phenomenological (Bruce et al. 1999a; 1999b; Macherey et al. 2007), in conductance-based (Badenhorst et al. 2016; Dangerfield et al. 2010; Goldwyn et al. 2011; Goldwyn and Shea-Brown 2011; Huang et al. 2013; Imennov and Rubinstein 2009; O'Brien 2016; Rattay et al. 2001b; Rubinstein 1995) and most recently in hybrid biophysical-phenomenological based (van Gendt et al. 2016; van Gendt et al. 2017) stochastic models. The majority of purely conductance-based stochastic models are applied on a single node of Ranvier due to their high computational cost compared to phenomenological and hybrid models

which are easily applied to full length fibres. However, only conductance-based or biophysical models, such as the HH based models, provide biophysically meaningful results (Izhikevich 2004) to evaluate the impact of physiological fibre attributes, such as fibre diameter, nodal and internodal lengths, and myelin thickness, in the study and modelling of CIs (Rattay et al. 2001b). Except for the Rattay model (Rattay et al. 2001a; Rattay et al. 2001b), the biophysical stochastic models that are applied on full fibres, are applied within a homogenous medium and not within 3D volume conductions models as is the objective in the present study.

The primary objective of the present study is to determine if the application of a biophysical stochastic population ANF model in a VC model of user-specific cochleae has a significant intra-user impact on excitation threshold and dynamic range compared to a single deterministic and stochastic fibre model. (*Intra*-user comparison, for the purpose of this study, is defined as comparing the predictions of a user's deterministic model with the same user's stochastic model as opposed to comparing it to other users' predictions (*inter*-user comparison)) Therefore, of the three types of purely conductance-based stochastic models identified and reviewed by Goldwyn and Shea-Brown (2011), a current noise method is used in this study due to it having the lowest computational cost for this initial investigation. The particular current noise method used is the voltage dependent current noise term and algorithm presented in Badenhorst et al. (2016) which has been shown to adhere to the measured stochastic fibre characteristics of a negative linear log(*Relative Spread*) vs log(*diameter*) distribution and the exponential distribution of the standard deviation of membrane noise (V_{rms}) versus transmembrane voltage (V_{mem}) (Verveen 1962; Verveen and Derksen 1968). Relative spread (*RS*) is defined as the standard deviation (σ) of the discharge probability function (DPF), also referred to as the threshold region width or spread, divided by the 50% discharge probability stimulus intensity (μ) of the DPF, a.k.a. the stochastic threshold (Rubinstein 1995; Verveen 1962). By keeping the stochastic model purely conductance-based, the origin of the stochasticity remains an inherent part of the ANF model through the membrane voltage (Verveen and Derksen 1968) and through the nodal surface area (via fibre diameter and nodal length), which accounts for the effect of the number of sodium channels per node on the noise magnitude (Badenhorst et al. 2016; Rubinstein 1995).

This article presents the application of a purely conductance-based stochastic nerve fibre model (Badenhorst et al. 2016) to a human ANF in a VC model of a semi-generic head and user-specific cochlea for four users. Section 2 provides the methodology in terms of the ANF morphology, VC modelling used, a brief overview of the stochastic conductance-based computational ANF model, creation of fibre population models and the validation criteria and procedures. Section 3 first provides graphical validation of the human compound ANF model in terms of a log(*RS*) vs log(*diameter*) analysis for all users with full and degenerate fibres, as well as the exponential membrane noise (V_{rms}) versus the transmembrane voltage (V_{mem}) distribution. Secondly, an intra- and inter-user modelled threshold comparison between single deterministic and stochastic fibres (full and degenerate) is presented, followed by a DPF comparison among four populations of fibres of one user for the cases of distributed and aligned somas with varying and uniform fibre diameters. Thirdly, selected temporal characteristics of the proposed model are validated against feline physiological measurements to ensure that these temporal ANF characteristics are modelled correctly. Characteristics are evaluated using discharge rate, latency and latency standard deviation vs stimulus intensity plots, as well as period and ISI histograms. The article then concludes with a brief discussion of the results obtained and future application of the model.

2. Methodology

2.1. ANF morphology

The study used the HH-based human compartmental ANF model of Rattay et al. (2001b), except for the dendrite's internodal distances which were scaled in accordance with the method presented in Kalkman et al. (2014). The resulting morphology in Fig. 1 shows the assigned node numbers that represent the unmyelinated or active compartments, as well as the original compartment numbers and lengths. The scaling of the dendrite in the user-specific VC models of the cochleae ensured the correct anatomical location of the dendritic terminal nodes at the lateral edge of the spiral lamina and of the soma in Rosenthal's canal (Kalkman et al. 2014). Scaling also enabled the Rattay model to produce propagating action potentials (APs) at a modelling temperature of 37°C.

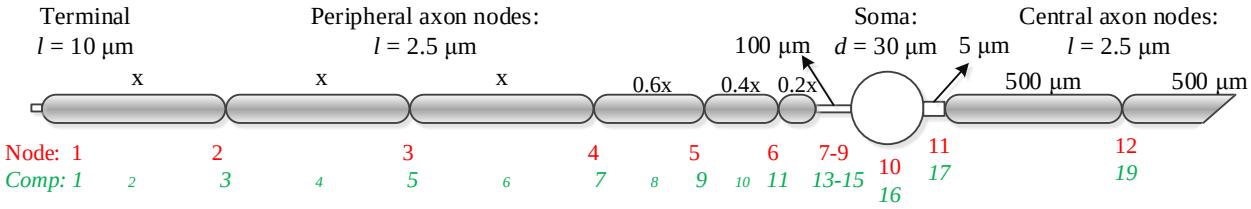

Fig. 1 A representation of the human ANF morphology showing nodal and compartmental diameters, lengths and numbers as in Rattay et al. (2001b), except for the scaled dendrite internodal distances which is a function of *x* as presented in Kalkman et al. (2014) to ensure the correct anatomical location of the dendritic terminal nodes at the lateral edge of the spiral lamina and of the soma within Rosenthal's canal

An average axon diameter of d_{avg} = 3 µm was used in most simulations based on the weighted average diameter calculated from the physiological data in Fig. 15 of Spoendlin and Schrott (1989) in which the axon diameter (d_{axon}) varies between 2 µm and 5 µm. In all simulations the dendrite diameter was set to half the axon diameter (Rattay et al. 2013) and the nodes of Ranvier kept at a length of 2.5 µm in accordance with the Rattay model. The majority of simulations, in particular those analysing the temporal characteristics, were done for degenerate fibres only, as it has been shown in both clinical and experimental studies that the majority of cochleae of people with profound hearing loss show moderate to complete degeneration of the dendrite (Lu and Schuknecht 1994; Nadol et al. 1989; Nadol Jr 1990; Otte et al. 1978). Though it is known that degeneration of the ANF begins at the dendrite and progresses toward the soma and axon (Felder et al. 1997; Nadol Jr 1990; Shepherd and Javel 1997) and that electrical stimulation of the surviving ANFs do not prevent degeneration (Agterberg et al. 2010; Coco et al. 2007), it has also been found that the majority of somas survive (Nadol et al. 1989; Otte et al. 1978). Hence degenerate fibres were created by terminating the dendrites at node 5 (compartment 9) of Fig. 1 thereby including the surviving soma into the degenerate ANF.

2.2. Volume conduction models and stimuli

The ANF model was applied in four user-specific cochlea VC models, of which a MATLAB rendition is shown in Fig. 2. Each cochlea was positioned within a semi-generic head VC model (Fig. 3) based on the work by Malherbe (2009), Malherbe et al. (2013) and Malherbe et al. (2015) to form user-specific compound models. The head model, developed in COMSOL, provides the potential distribution upon electrical stimulation within the cochlea and in particular, via interpolation using the MATLAB-COMSOL interface, at the centre of each of the fibres' compartments. A detailed explanation of the process is found in Briaire and Frijns (2005). These compartment potentials serve as input to the conductance-based computational ANF model to determine if the particular stimulus causes the fibre to be excited and produce a propagating AP or not. A bone conductance of 0.0154 S/m

was used and single fibres were spaced at 5° intervals around the modiolus following a radial pattern from the modiolus into and through the centre of the spiral lamina. Somas of these fibres were positioned approximately in the centre of Rosenthal's canal (Malherbe et al. 2015).

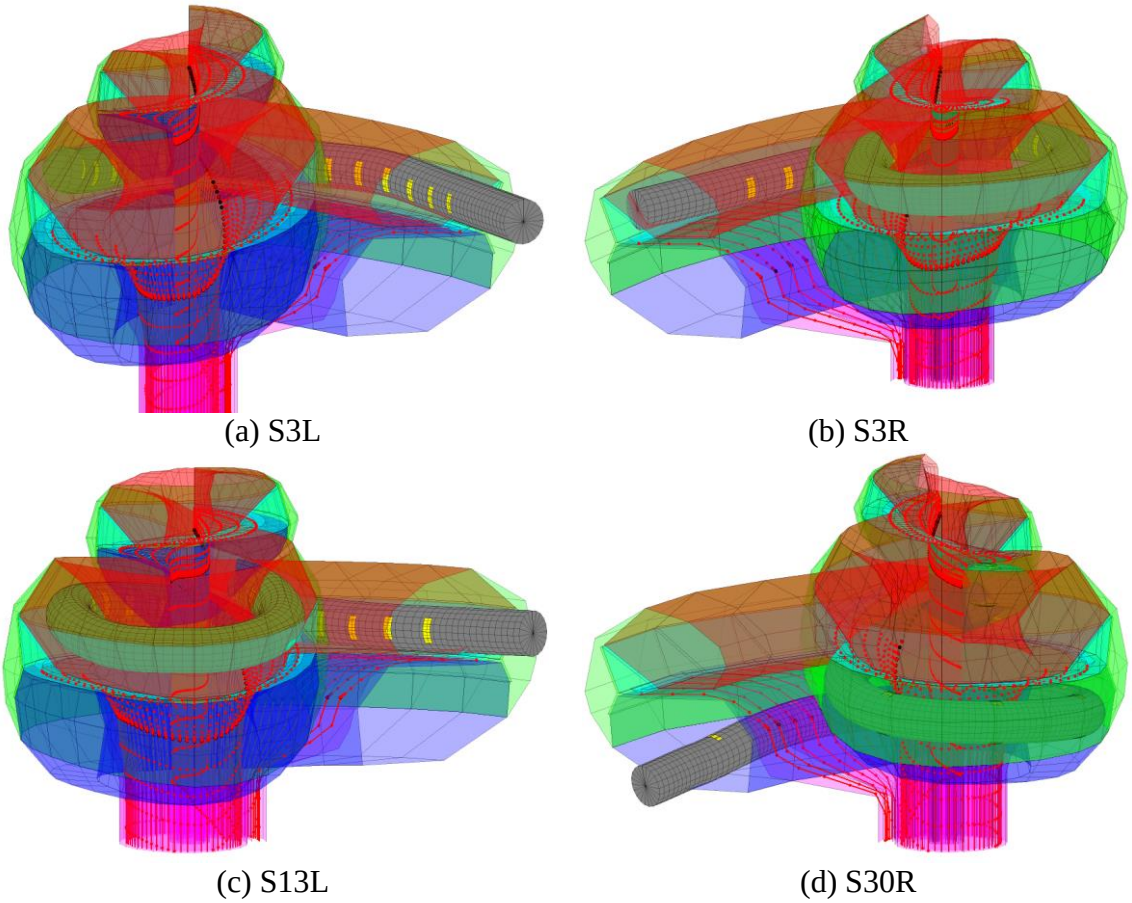

(a) S3L (b) S3R

(c) S13L (d) S30R

Fig. 2 User-specific cochlea VC models rendered in MATLAB and labelled as 'S' for user, user number and 'R' for right cochlea or 'L' for left cochlea. Three of the users have scala vestibuli insertions, with S3L having a shallow insertion. Fibres are spaced at 5° intervals around the modiolus following a radial pattern from the modiolus into and through the centre of the spiral lamina. The somas of these fibres are located approximately in the centre of Rosenthal's canal

All stimuli were mono-polar, bi-phasic, cathodic first with pulse widths (PW) and inter-pulse widths (IPW) as specified in Table 1 for the user-specific scenario (as per their MAP settings) or for the alternative scenario to investigate the effect of a longer or shorter pulse width. All stimulus intensities are stated in dB re 1 μA.

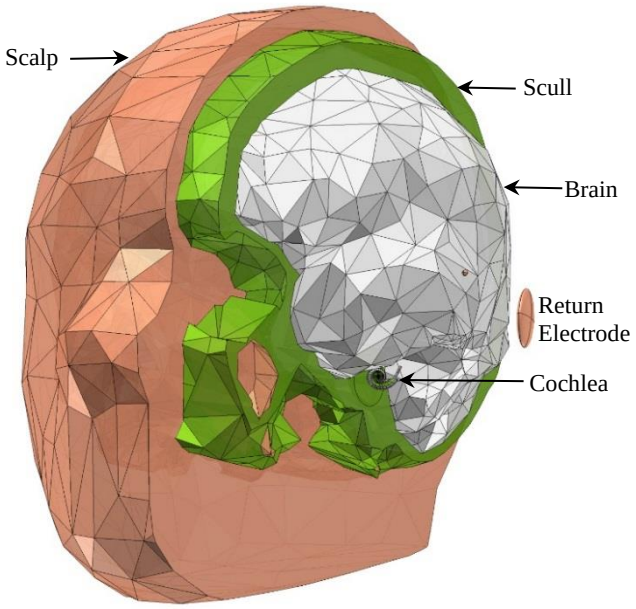

Fig. 3 COMSOL volume conduction model of the semi-generic head showing the location of a cochlea VC model and return electrode within the head

Table 1. User implant, insertion and stimulus settings (PW, IPW and pulses per second (pps)) according to their MAPs and the alternative PW used for investigating the effect of a longer or shorter PW.

User (subject) number, (L)eft or (R)ight ear.	**Implant**	**Insertion**	**User-specific (MAP setting)**			**Alternative**	
			PW [µs]	IPW [µs]	Pulse rate [pps]	pw [µs]	ipw [µs]
S13L	Cochlear®	Scala Vestibuli	25	8	900	85	0
S3R, S3L	Cochlear®	Scala Vestibuli	25	8	500	85	0
S30R (electrode 8)	MED-EL	Scala Tympani	85	0	750	25	8

2.3. Conductance-based stochastic computational ANF model

The stochastic HH-based Rattay ANF computational model (Rattay et al. 2001b) was implemented using the current noise term and voltage dependent current noise algorithm developed by Badenhorst et al. (2016). Figure 4 depicts the implementation of current noise in a section of a nerve fibre from which only a brief explanation of the parameters and principles required for this paper will be presented here. For a comprehensive description of the methodology and calculation of the various electrical components, currents and voltages the reader is referred to Rattay et al. (2001b), Rattay (1990) and Badenhorst et al. (2016).

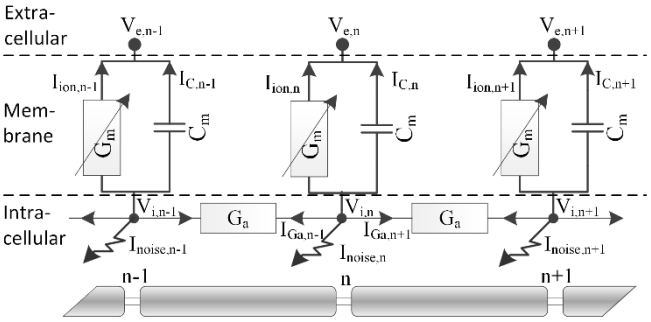

Fig. 4 A standard electrical cable network of a section of an ANF axon with three nodes (n) of Ranvier and internodal compartments. V_i and V_e respectively represents the intra- and extra- cellular potentials. Currents indicated are the membrane capacitance current I_C, the potassium, sodium and leakage HH ionic currents represented by I_{ion}, the axoplasmic currents I_G and the injected noise current I_{noise}. Electrical components shown are the axoplasmic conductance G_a, membrane capacitance C_m and voltage dependent membrane conductance G_m

Using Kirchoff's current law at node *n*, an expression for the membrane capacitance current, $I_{C,n}$, is obtained as:

$$I_{C,n} = C_m \frac{\delta V_{mem,n}}{\delta t} = -\left(I_{ion,n} + I_{noise,n}\right) + I_{st,n} \quad (1)$$

where $V_{mem,n}$ is the transmembrane voltage defined as the difference between the intra- and extracellular potentials $\left(V_{i,n} - V_{e,n}\right)$, $I_{ion,n}$ represents the ionic currents as defined by HH, $I_{st,n}$ represents the axoplasmic currents $\left(-I_{Ga,n-1} - I_{Ga,n+1}\right)$ and $I_{noise,n}$ the added Gaussian noise current as defined in Eq. (2) and (3) .

$$I_{noise,n} = GAUSS \cdot \frac{k_{fact,n} \cdot 10^{-8}}{\sqrt{A_n \cdot g_{Na}}} \times SF \quad (2)$$

$$SF = 4.0 \times \left(\frac{d_{axon}}{d_{avg}}\right)^{-1.4} \quad (3)$$

GAUSS is a random variable with a standard normal distribution ($\mu = 0$, $\sigma = 1$) of which the value changes every 1 μs (compared to the 2.5 μs in Rattay et al. (2001b)), k_{fact} is a noise factor which is a function of both the unmyelinated axon diameter (d_{axon}) and V_{mem} as per the voltage dependent current noise algorithm in Badenhorst et al. (2016), g_{Na} is the maximum sodium conductance density and A_n is the membrane surface area of node *n*. The scaling factor (*SF*) defined in Eq. (3) is the *SF* to be used in Eq. (2) for an axon having a diameter 2 μm $\leq d_{axon} \leq$ 5 μm compared to the average axon diameter of d_{avg} = 3 μm. To compare the temporal characteristics of the stochastic human ANF model to those physiologically measured in felines, the coefficient in Eq. (3) was reduced from the original 4.62 used in the cat ANF model to 4.0 and the exponent rounded from -1.43 to -1.4 as discussed and illustrated in Section 3.1.

The addition of the Gaussian current noise term of Eq. (2) as shown in Eq. (1), results in the HH system of *ordinary* differential equations (ODEs) being converted into a system of *stochastic* differential equations (SDEs). The system can therefore not be solved using ODE numeric solvers and hence a first order implicit Euler-Maruyama numerical method based on Itô-calculus was implemented in MATLAB to obtain a valid SDE numerical solver (Govender 2006; Higham 2001). A fixed time step-size of 1 μs was used in the numerical SDE solver to correspond with the noise values changing every 1 μs.

2.4. Verification of the human stochastic ANF model characteristics

One of the important characteristics of a stochastic fibre is its negative linear log(*Relative Spread*) vs. log(*diameter*) distribution as measured by Verveen (1962). This characteristic is verified in Section 3.2 for each of the four user-specific compound models to ensure that the stochastic compound human ANF model presented, correctly models this measured physiological characteristic as was the case in the feline ANF model in Badenhorst et al. (2016). First, an electrode was identified within each model that lies at approximately the same angle within the cochlea relative to the start of the basal turn. Secondly, of the single fibres shown in Fig. 2, the full and degenerate fibre having the

lowest deterministic threshold at d_{avg} for each of these stimulating electrodes was determined. This could result in the fibre identified not being tonotopically aligned with the stimulating electrode, especially in the case of degenerate fibres. Thirdly, the DPFs for these fibres were generated at d_{axon} = 2, 2.5, 3, 4 and 5 μm from which the log(*RS*) vs log(d_{axon}) distribution was finally generated for each user model and fibre.

A second characteristic of a stochastic fibre is the exponential distribution of the standard deviation of membrane noise (V_{rms}) versus the transmembrane voltage (V_{mem}) as measured in Verveen and Derksen (1968). This characteristic is verified for the human ANF of a single user in Section 3.2 by extracting and plotting V_{rms} versus V_{mem} as described in Badenhorst et al. (2016).

2.5. Threshold comparison between single fibres and populations of deterministic and stochastic fibres

To determine if the addition of stochasticity has a significant impact on fibre thresholds, the deterministic thresholds of each of the fibres identified for the log-log distribution tests are compared to one another and to their corresponding stochastic thresholds at d_{avg} in Section 3.3.1. The stochastic threshold of a fibre is defined as the stimulus intensity corresponding to a discharge probability of 50%, (Verveen 1962).

To investigate the effect of varying the diameter, position (i.e. electrode-fibre separation) and soma location of a fibre, a comparison is also made (Section 3.3.2) between thresholds and DPF spreads of four populations of fibres for a single user. All four populations were formed by first replacing the single degenerate fibre of user S3L identified for the log-log distribution tests, shown in Fig. 5a, with 18 degenerate fibres as illustrated in Fig. 5b and Fig. 5c. Since the single fibres in Fig. 2 are spaced at 5° intervals around the modiolus, the trajectories of the fibres in the population were uniformly spread within a radial arc of slightly less than 5° (2.5° toward the apex and 2.5° toward the base from the single fibre's location) using a version of Lloyd's algorithm for approximating a centroidal Voronoi tessellation [1] (Du et al. 1999). The predictions for the single degenerate fibre was used as a benchmark against which to compare the fibre population's predictions. Figure 5d shows the position of the populations relative to the actual stimulating electrode selected as described in Section 2.4 and shown in Section 3.2. It should be noted in Fig. 5d that the fibre population is not tonotopically aligned with the stimulating electrode.

The first of the four populations was subsequently created by distributing the somas along the fibre trajectories within Rosenthal's canal and positioning the nodes of Ranvier relative to the soma along the fibre trajectory in accordance with the morphology in Fig. 1. This is illustrated in Fig. 5b. Somatic diameters were all set to 30 μm while axon diameters were randomly selected such that 2 μm $\leq d_{axon} \leq$ 5 μm in proportion to the distribution of the measured diameters in Spoendlin and Schrott (1989). The second of the four populations was formed by setting all axon diameters of population 1 to d_{avg}. Population 3 was formed by aligning the somas to approximately the same position as that of the original single fibre within Rosenthal's canal as shown in Fig. 5c and assigning the same fibre diameters of population 1 as per Fig. 6. Similar to population 2, population 4 was formed by setting all axon diameters to d_{avg}. An alternative method for creating a population of fibres is presented by Kalkman et al. (2015).

[1] http://math.stackexchange.com/questions/366474/find-coordinates-of-n-points-uniformly-distributed-in-a-rectangle

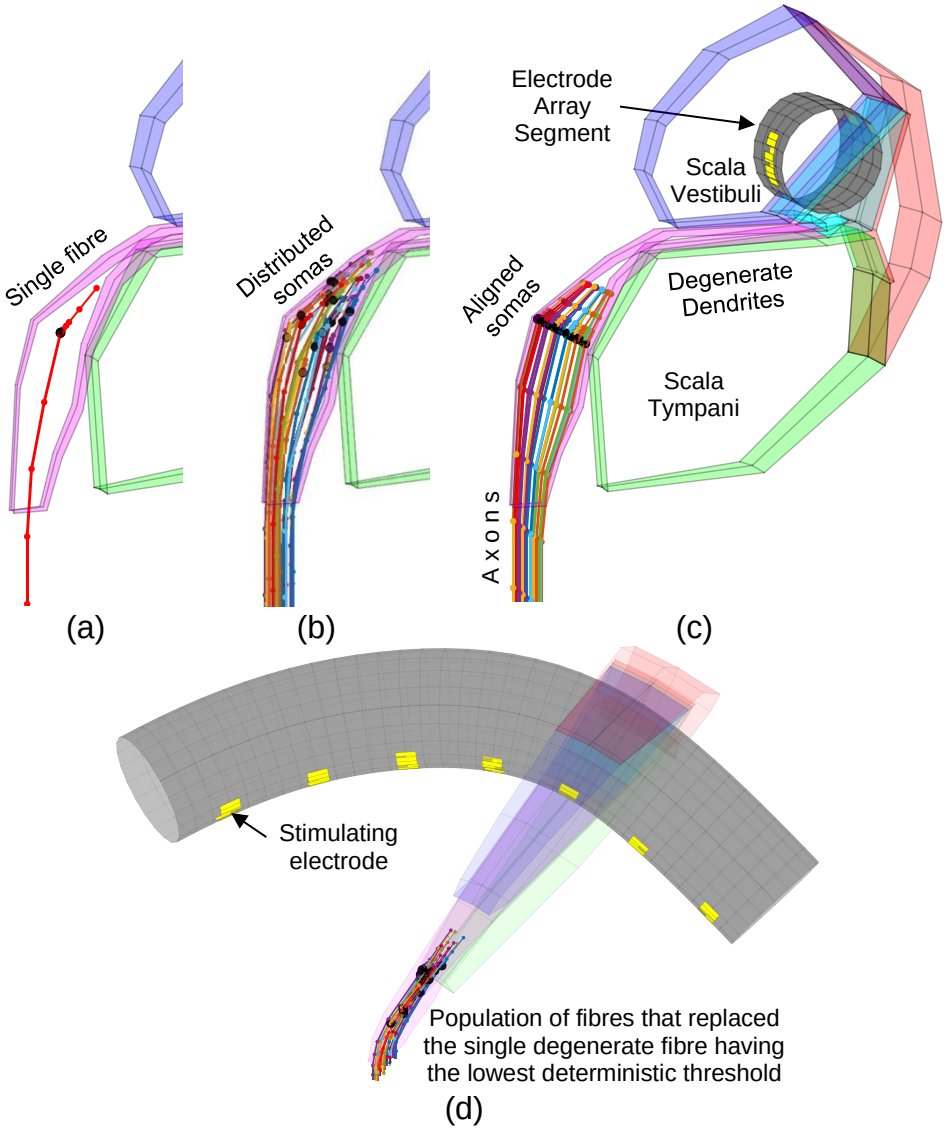

Fig. 5 (a) The single degenerate fibre of user S3L identified from Fig. 2a for the log-log distribution tests of S3L having been replaced by populations of 18 uniformly spread fibres shown in (b) and (c) to investigate the effect of varying the diameter, position and soma location of a fibre. The larger, black dot indicates the position of the soma while the smaller dots indicate the node of Ranvier locations. (b) Populations 1 and 2 have distributed somas within Rosenthal's canal along the fibre trajectories with somatic diameters of 30 µm. Axon diameters for population 1 vary between 2 µm and 5 µm (as shown in Fig. 6) in proportion to the distribution of the measured diameters in Spoendlin and Schrott (1989) while all fibres in population 2 have a diameter of 3 µm. (c) Populations 3 and 4 have somas aligned within Rosenthal's canal with axon diameters the same as for populations 1 and 2 respectively. (d) Top view of population 1 showing its position relative to the stimulating electrode as selected in Section 3.2. It should be noted that the fibre population is not tonotopically aligned with the stimulating electrode and that the electrode shown in (c) is not the stimulating electrode

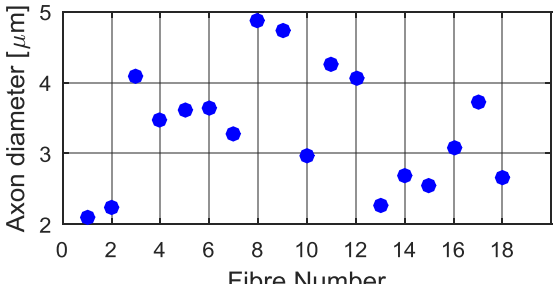

Fig. 6 Axon diameters for each of the 18 fibres in populations 1 and 3 of Fig. 5b and Fig. 5c respectively

2.6. Temporal validation of the stochastic fibre model

A final validation of the conductance-based stochastic compound human ANF model was done by generating discharge rate, latency and latency standard deviation versus stimulus intensity plots, as well as period and ISI histograms using the stochastic, degenerate fibres identified for and used in the log-log distribution tests. Simulations were done at PWs of 25 µs and 85 µs and using pulse-trains at rates of between 200 and 1100 pps/ch based on the user's MAP settings, preferences and pulse rates used in experiments (Arora et al. 2009; Fu and Shannon 2000; Vandali et al. 2000; Xu et al. 1997). Latency was measured as the time between stimulus onset and the peak of the first AP on the ANF. The graphs are presented in a format similar to the physiological data for cat in Javel and Shepherd (2000) for ease of comparison and validation.

3. Results

3.1. Motivation for the chosen *SF* coefficient and exponent values

It was noted in Badenhorst et al. (2016) that *in vivo* measurements of human ANFs do not exist against which to verify the DPF spread and hence the coefficient of 4.62 and exponent of -1.43 in the *SF* function in Eq. (3), SF_0 , only serve as initial estimates. The DPF with solid markers in Fig. 7 is the result of the application of SF_0 to a full fibre of user S3R at d_{axon} = 2 µm. A DPF is the least squares fit to a cumulative Gaussian function as represented by 15 discharge probabilities (markers), calculated as the number of discharges out of 100 simulations of a single pulse, at 15 stimulus intensity levels. The simulated probabilities (markers) are noted to reach unity at a higher stimulus intensity (68.5 dB) than that of their fitted DPF (line, 66 dB). This was found to be due to the large *SF* value at the small diameter causing the magnitude of the noise to be high enough to inhibit the generation of APs at the higher stimulus intensities where the probability should have been one, according to the fitted DPF. Evaluation of *in vivo* measured DPFs of feline ANFs however show that this phenomenon is an artifact of the model, since it does not occur in actual ANFs, and that the measured probabilities reach a steady unity state along with the fitted DPFs (Javel and Shepherd 2000; Shepherd and Javel 1997; Shepherd and Javel 1999).

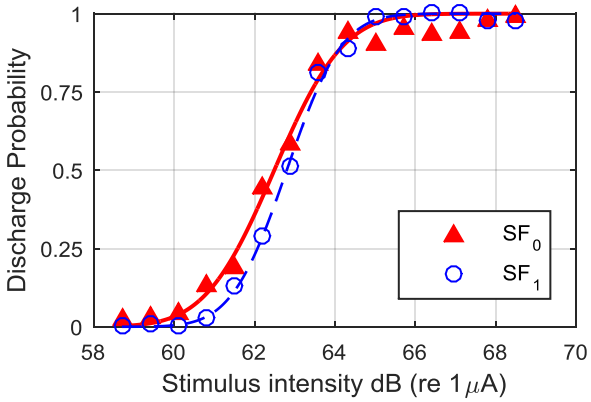

Fig. 7 Simulated discharge probabilities and least square fitted DPFs of an ANF in user S3R at d_{axon} = 2 µm for the case where the *SF* coefficient and exponent in Eq. (3) are 4.62 and -1.43 respectively, SF_0, and for the case where the *SF* coefficient and exponent have been reduced to 4.0 and -1.4 respectively, SF_1. The probabilities for SF_0 are prevented from reaching unity at the same stimulus level as the fitted DPF owing to the large *SF* value causing a high enough noise magnitude to inhibit the generation of APs. A reduction of the coefficient to 4.0 in SF_1 solves this deviation from measured feline ANF discharge probabilities and DPFs. The probability represented by each marker was calculated as the average probability out of 100 simulations at the particular stimulus intensity

The coefficient of the *SF* function was therefore decreased to 4.0 and the exponent rounded to -1.4, SF_1, which resulted in the modelled probabilities (open markers) in Fig. 7 reaching unity along with its fitted DPF (broken line) having a slightly lower spread and higher stochastic threshold. Figure 8 shows the *SF* values of both cases for 2 µm ≤ d_{axon} ≤ 5 µm in which it is noted that the difference in *SF* values for SF_0 and of SF_1 is relatively small and decreasing as the diameter increases.

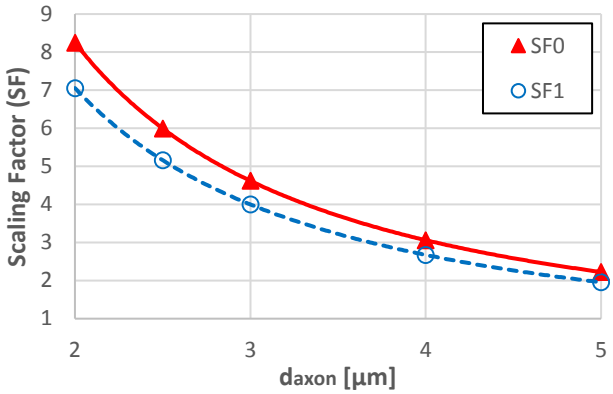

Fig. 8 Current noise *SF* values of Eq. (3) for SF_0 and SF_1 versus axon diameter show a relative small difference in *SF* values, which decreases as the diameter increases

3.2. Validation of the negative linear log(*RS*) vs log(d_{axon}) and exponential V_{rms} vs V_{mem} characteristics

Figure 9 shows the relative electrode array trajectories, electrode locations (markers) and selected electrodes (encircled and numbered in the legend) of the four user-specific models as viewed down the centre axis of the modiolus. Electrode numbering for the implants of users S3R and S13L starts from 1 at the basal end of the array and at 8 for user S3L due to a shallow insertion thereby excluding electrodes 1 to 7 from the model and figure. For user S30R, having an MED-EL implant, numbering starts from 1 at the apical end of the array.

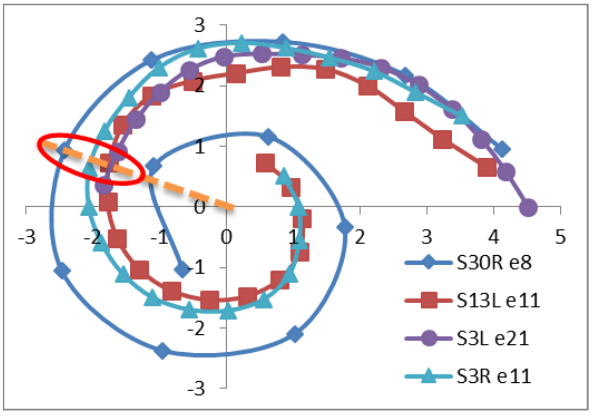

Fig. 9 Top view down the modiolus of the electrode array trajectories for the four users with the encircled electrodes along the broken radial line selected for the log(*RS*) vs log(d_{axon}) distribution tests. The selected user-specific electrode numbers are given in the legend (example e21 for electrode 21) and axes units are in millimetres

The DPF and log(*RS*) vs log(d_{axon}) results for the fibre having the lowest deterministic threshold for each user's selected electrode are presented in Fig. 10a for the case of all fibres in Fig. 2 being full fibres and in Fig. 10b for the case of all fibres being degenerate fibres. It is therefore important to note that, except for user S30R, the degenerate fibre evaluated in Fig. 10 and subsequent results is not the same physical fibre at the same location as the full fibre. User-specific stimuli were used as per Table 1. In all cases the stochastic threshold and spread of the DPFs decrease for an increase in diameter, resulting in the required negative linear log(*RS*) vs log(d_{axon}) distribution. The conductance-

based stochastic compound human ANF model therefore conforms to this important stochastic nerve characteristic as discovered by Verveen (1962) .

Comparing full fibre to degenerate fibre thresholds, users S3R, S3L and S13L show an increase of approximately 3 dB for the degenerate fibres while user S30R shows near identical predictions for the full and degenerate fibres. It was found that the site of AP initiation for user S30R is on the axon for both the full and degenerate fibre, whereas the other users' site of initiation is on the dendrite for the full fibre and on the axon for the degenerate fibre. This correlates well with the knowledge that S30R has a scala tympani insertion in which the electrode is nearer to the axon compared to the scala vestibuli insertions of the first three users, in which the electrode is nearer to the dendrite.

The exponential V_{rms} versus V_{mem} characteristic is verified in Fig. 11 using a straight ANF (d_{axon} = 3 µm) with a bi-phasic (PW = 200 µs), cathodic first stimulus on a single monopolar point electrode above node 4 in an infinite homogeneous medium (ρ_e = 0.3 kΩ·cm). The open markers represent V_{rms} resulting from the applied voltage dependent current noise algorithm and Eqs. (2) and (3) at the modelled nodal surface area A_n. The dendrite noise is seen to be higher than the axon's due to the dendrites smaller diameter and hence smaller A_n. If the noise is downscaled back to its original value to correspond to the estimated average nodal surface area of the fibres measured in Verveen and Derksen (1968), A_0, the solid markers are a near perfect fit to their measured noise curve (VD data).

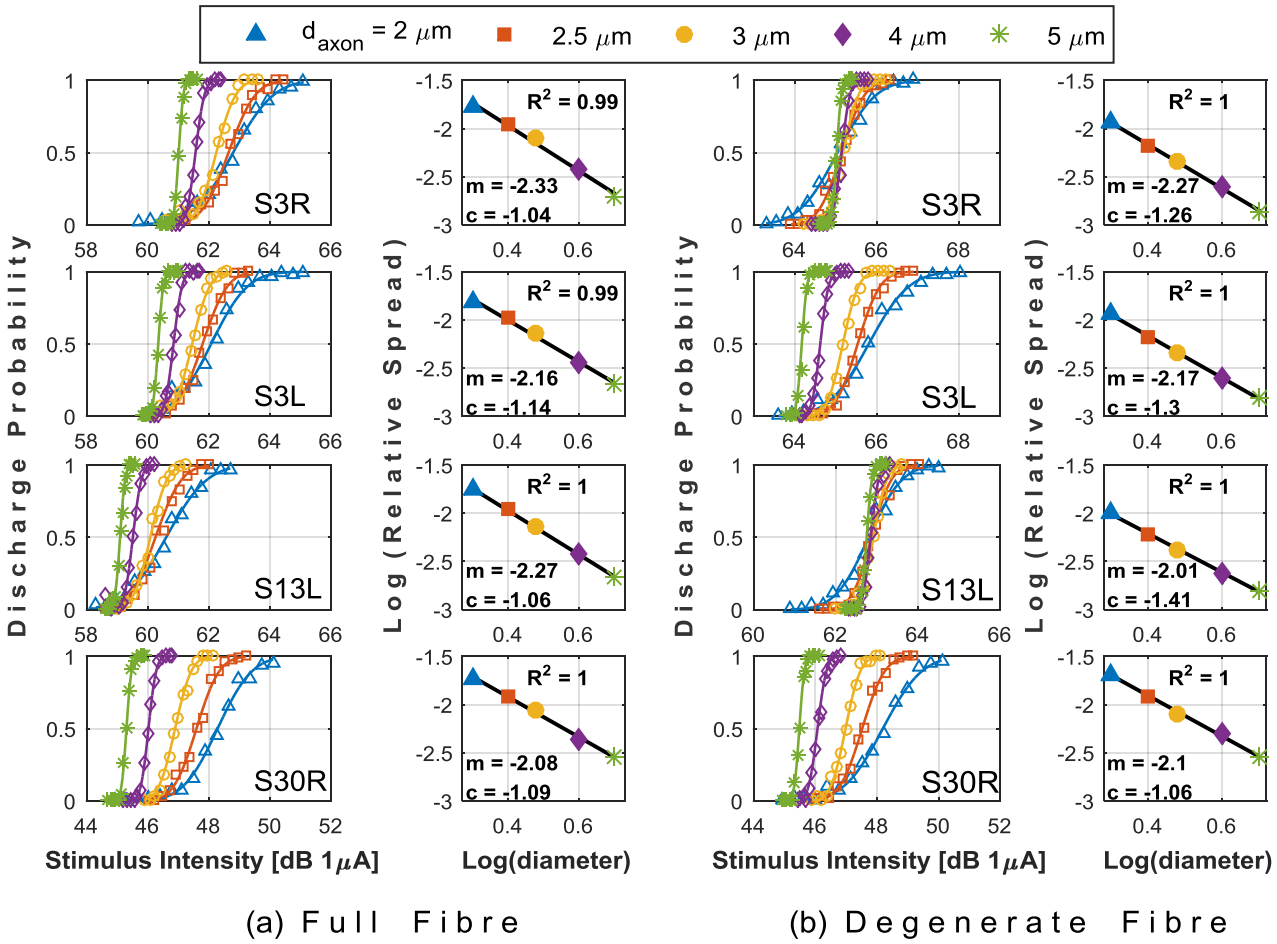

Fig. 10 User-specific DPFs and their corresponding log(*RS*) vs log(d_{axon}) distributions for (a) full and (b) degenerate fibres. DPFs show the required decrease in spread or standard deviation along with a decrease in stochastic threshold with an increase in diameter. The corresponding log-log distributions all show near perfect least square negative linear fits as required with gradients (m) and intercepts (c) given for each distribution. User-specific PWs were used as per Table 1

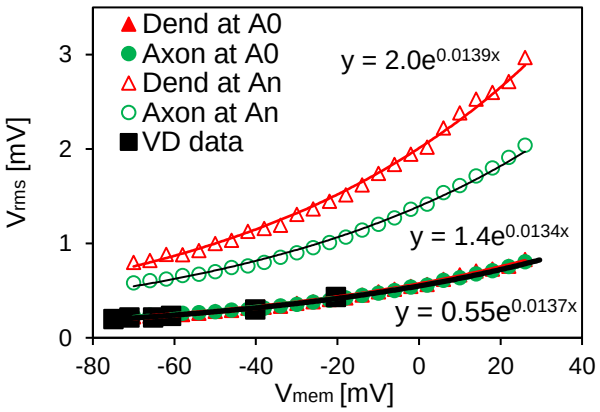

Fig. 11 The modelled membrane noise (V_{rms}) versus transmembrane voltage (V_{mem}) at a modelled nodal area A_n (open markers) exhibits an exponential distribution as measured by Verveen and Derksen (1968). If "unscaled" to the estimated average nodal surface area of the fibres measured in Verveen and Derksen (1968), A_0, the solid markers are a near perfect fit to their measured noise curve (VD data)

3.3. Threshold comparison of deterministic and stochastic fibres

3.3.1. Single fibres

Deterministic (vertical lines) and stochastic (DPF at P = 0.5) thresholds are compared intra- and inter-user in Fig. 12 for full (top) and degenerate (bottom) ANFs at a short (left) and long (right) PW. An increase in PW results in a decrease in thresholds for all users as expected (Javel et al. 1987; Shepherd and Javel 1999). Except for user S30R whose site of AP initiation was found to be on the axon even for a full fibre, degenerate fibres show an increase in threshold due to the site of AP initiation shifting from the now degenerate dendrite, which is nearer to the stimulating electrode, to the axon which is further (Javel et al. 1987; Rattay 1987). Apart from the full fibres at PW = 85 µs (Fig. 12b), the differences between the deterministic and stochastic thresholds are negligible and fibres have a small dynamic range. Dynamic range is defined as the intensity range over which the discharge probability increases from 0.1 to 0.9 (Shepherd and Javel 1997).

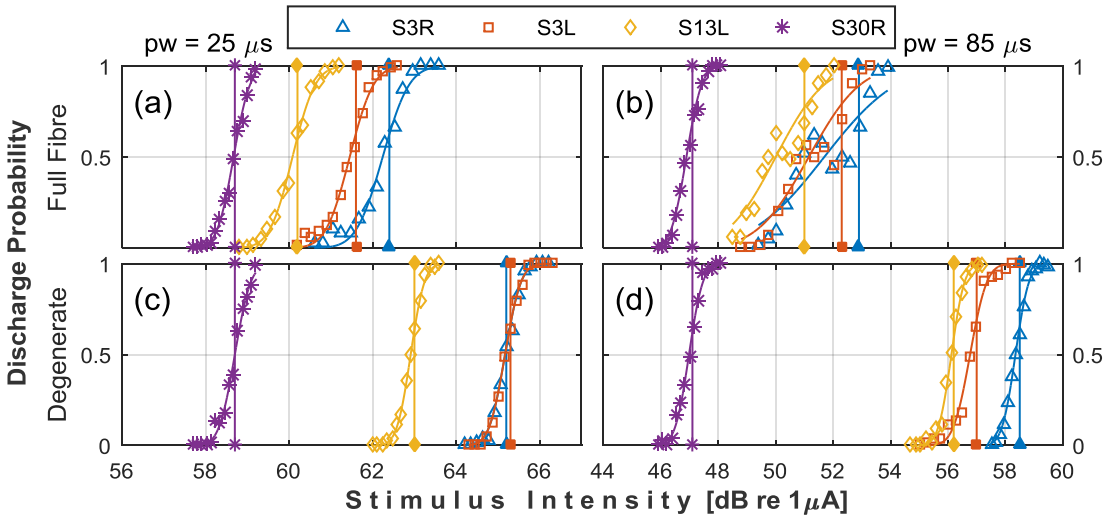

Fig. 12 User-specific deterministic vs stochastic threshold comparison for full (top) and degenerate (bottom) fibres at 25 µs (left) and 85 µs (right) pulse widths. Fibres show a significant decrease in threshold at the long pulse width for all users. Except for S30R whose site of AP initiation is on the axon even for the full fibre scenario, degenerate fibres have slightly higher thresholds for both pulse widths. DPFs in (b) show non-normal distributions because of a model artifact in the deterministic full fibre model resulting in a seemingly larger dynamic range in fibre excitation

Closer inspection of the DPFs of the full fibres at PW = 85 µs in Fig. 12b reveals non-normal distributions of the discharge probabilities compared to their least-squares normal fits for users S3R, S3L and S13L that result in seemingly larger dynamic ranges in fibre excitation. This is shown more clearly in Fig.13 for user S3R in that the discharge probabilities initially follow a normal distribution up to 51 dB but then begin to decrease until a new normal distribution is followed from 52.7 dB onwards. Upon further investigation it was found that the cause of the non-normal distributions probably occurs in the deterministic model and in the dendritic compartments. Figure 13 (top) shows that although a propagating AP was initiated on the dendrite of the deterministic fibre from 50.93 dB to 51.96 dB and again above 52.90 dB, the AP could not propagate across the somatic nodes (dark, concentrated lines) from 51.97 dB to 52.89 dB. Since this "deadband" exists in the absence of stochasticity, the non-normal DPF distribution phenomenon must have its origin partly in the deterministic model. Simulation of other electrodes and fibres at PW = 25 µs also resulted in non-normal DPF distributions, but never for a degenerate fibre, as can be seen in Fig. 12d in which all DPFs have a normal distribution. This, together with the observation that the APs do not propagate across the somatic nodes within the deadband, supports the hypothesis that the phenomenon must also have its origin partly in the dendritic compartments. A change in soma diameter had a negligible effect on the deadband width and this phenomenon did not occur for the straight, full fibre in an infinite homogenous medium.

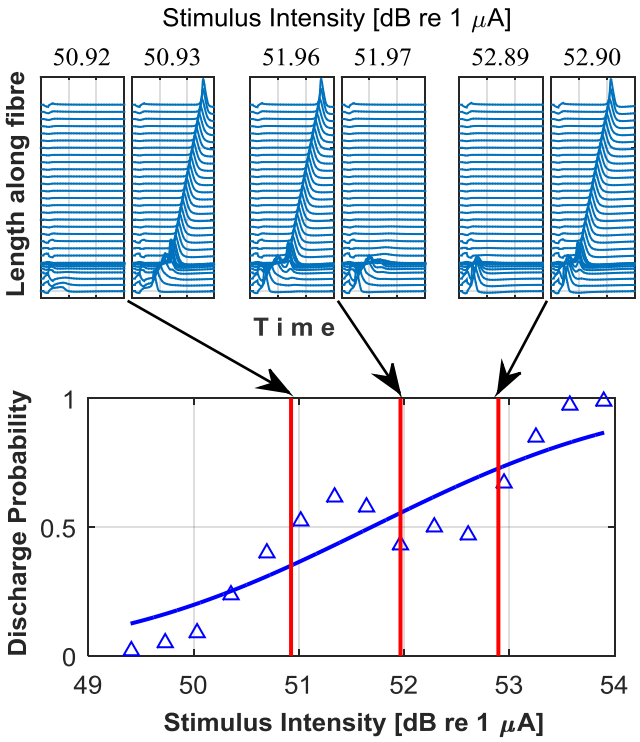

Fig. 13 (Top) Deterministic propagating action potentials along the full fibre of user S3R at PW = 85 µs showing a deadband region from 51.97 dB and 52.89 dB where the AP initiated on the dendrite does not propagate across the somatic nodes (dark, concentrated lines) even though it did propagate between 50.93 dB and 51.96 dB. (Bottom) DPF of user S3R from Fig. 12b with vertical lines at the three deterministic threshold transition stimulus levels (top) clearly showing that the deviation from a normal DPF distribution occurs around the deadband region

The cause of this phenomenon therefore seems to be a combination of the dendrite morphology and the volume conduction model. However, having already noted from literature that the majority of fibres of cochleae show moderate to complete degeneration of the dendrite, finding the actual cause of the phenomenon or model artifact was left for later investigation and the remaining simulations were only done for degenerate fibres in which the non-normal DPF phenomenon does not occur.

3.3.2. Population of fibres

The DPFs for the case of distributed somas of populations 1 and 2 are shown for varying fibre diameters (as per Fig. 6) in Fig. 14a and for all fibres having a diameter of 3 μm in Fig. 14b respectively. Similarly, Fig. 15a and Fig. 15b show the DPFs for populations 3 and 4 respectively, in which the somas are aligned within Rosenthal's canal in an attempt to minimise the effect of soma position. A few arrows indicate which DPFs are for the same fibres in (a) and (b) with the specific fibre number within the population alongside each arrow line. The thick, dashed DPF labelled "*50% Pop DPF*" in each of the figures represents the probability of 50% of the fibres in the population discharging at a given stimulus intensity thus, providing what will be referred to as a population (stochastic) threshold and DPF. The thick, solid, vertical lines at 65.26 dB and DPF in each of the figures respectively represent the deterministic threshold and stochastic DPF of the original single fibre (Fig. 5a) as first presented in Fig. 12c. Since the original single fibre, which is no longer present having been replaced by the population of fibres, would have been located in the centre of the population, one would expect its threshold and DPF to be located approximately within the centre of the DPF's of the population's fibres. This is indeed the case as seen in Fig. 14 and Fig. 15.

Variance in fibre diameter in Fig. 14a and Fig. 15a is manifested in a visible variance in DPF spread ($0.11 \leq \sigma \leq 0.72$) where larger spread or smaller gradients result from smaller diameters and *vice versa*. Upon changing the varying fibre diameters in (a) to 3 μm in (b), variance in spread becomes almost imperceptible ($0.27 \leq \sigma \leq 0.39$), while shifts in stochastic threshold are comparable with the dynamic range of the fibres. These two observations are better illustrated and discussed in Fig. 16.

Fig. 14 (Nest page) Each DPF, normally fitted to a set of 10 markers or probabilities, represents one of the 18 fibres within the fibre population of Fig. 5b for varying fibre diameters in (a) and a uniform 3 μm diameter in (b). The thick, dashed DPFs labelled "50% Pop DPF" represent the probability of 50% of the fibres discharging at a given stimulus intensity, while the thick, solid, vertical lines at 65.26 dB and DPF respectively represent the deterministic threshold and stochastic DPF of the original single fibre (Fig. 5a), as in Fig.12c. Arrows, numbered according to the specific fibre number in the population of Fig. 5b, indicate the shift of the fibre's DPF as a result of the fibre diameter (as per Fig. 6) in (a) having been changed to 3 μm in (b). A decrease in threshold and spread from (a) to (b) implies an increase in fibre diameter from (a) to (b) and *vice versa*, as confirmed in Fig. 16. The variance in diameters resulted in a visible variance in DPF spread in (a), whereas the uniform 3 μm diameter resulted in DPFs with a uniform spread in (b) with an almost insignificant change in thresholds relative to (a). Because all fibres in (b) have the same diameter, the variance in threshold in (b) must be because of the variance in fibre and soma location relative to the stimulating electrode. The threshold range of the population shows a slight decrease from approximately 5 dB in (a) to 4.3 dB in (b), while the 50% population DPFs shows an insignificant increase in the population threshold from (a) to (b)

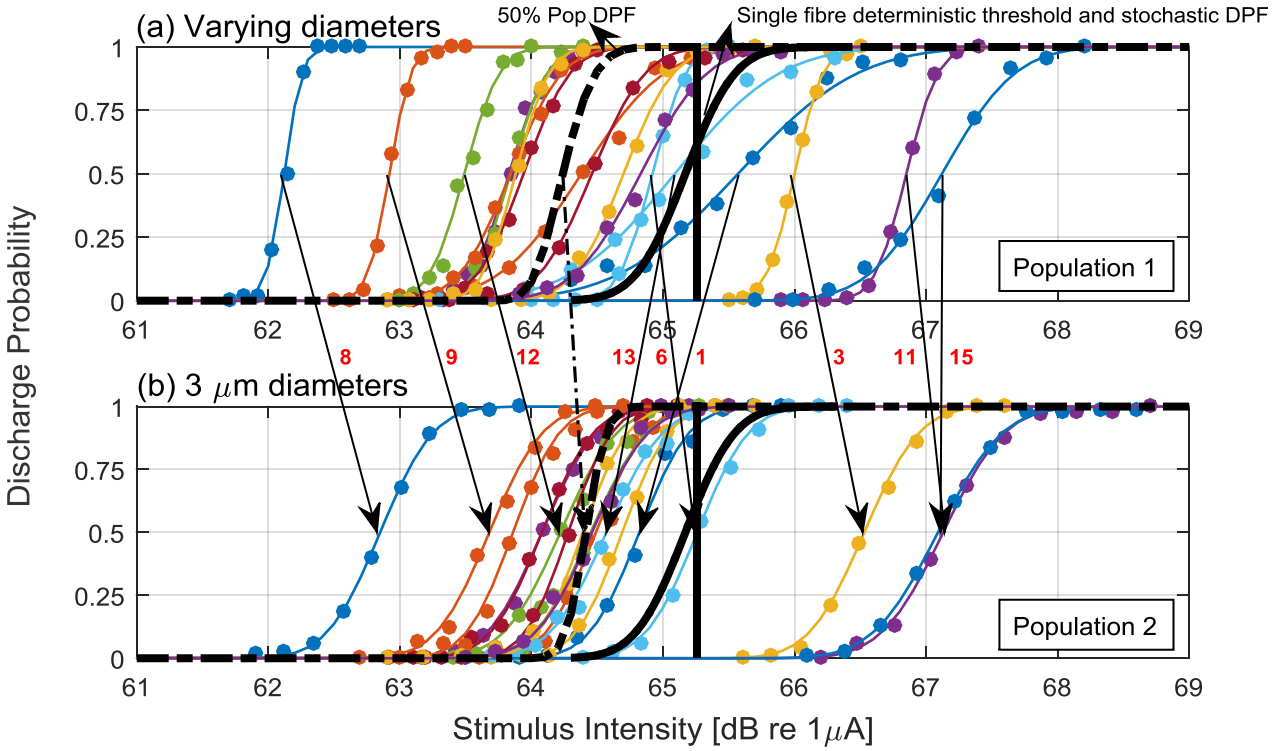

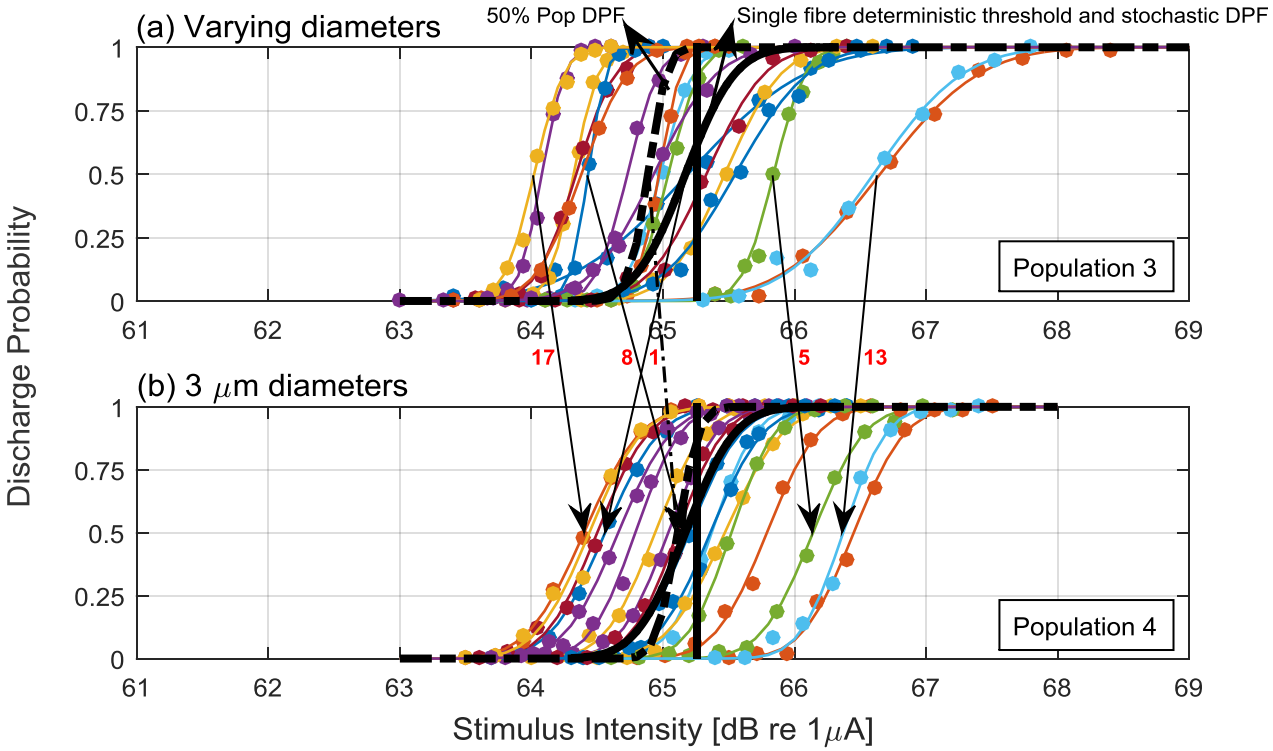

Fig. 15 Similar to Fig. 14, each DPF represents one of the 18 fibres within the fibre population of Fig. 5c (aligned somas) for varying fibre diameters in (a) and uniform 3 µm diameters in (b). Comparing Fig. 14 to Fig. 15 primarily shows that aligning the somas resulted in a noticeable decrease in the populations' threshold range: from 5 dB to 2.6 dB in (a) and from 4.3 dB to 2.0 dB in (b). This further supports the observation that the location of the somas affects the threshold of the fibres. The same observations are made regarding spread and threshold relative to fibre diameter, the 50% population DPFs and the population's threshold range as in Fig. 14 (distributed somas)

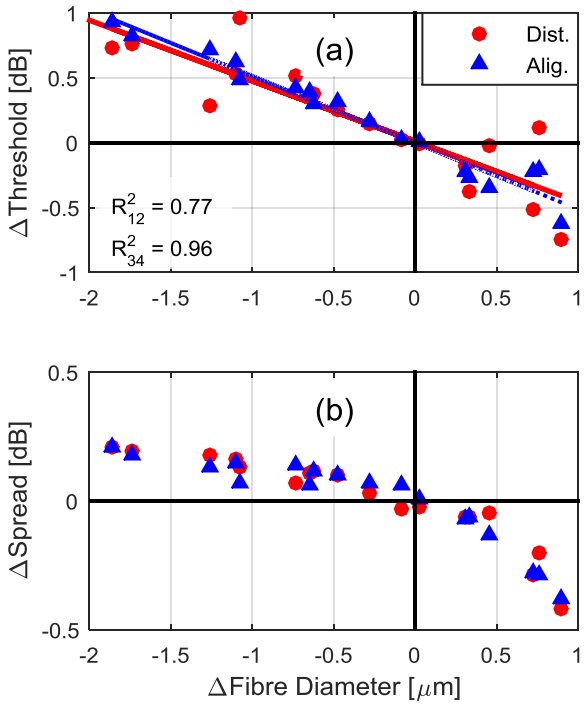

Fig. 16 (a) A decrease in the fibre diameter from d_a in both Fig. 14a (Dist.) and Fig. 15a (Alig.) to 3 µm in Fig. 14b and Fig. 15b ($\Delta d = 3 - d_a < 0$), results in an increase in the fibre threshold from μ_a in Fig. 14a and Fig. 15a to μ_b in Fig. 14b and Fig. 15b ($\Delta\mu = \mu_b - \mu_a > 0$), and *vice versa*. This corresponds to physiological measurements. (b) A decrease in fibre diameter ($\Delta d < 0$) results in a seemingly inverse exponential increase in DPF spread ($\Delta\sigma > 0$). A decrease in the fibre diameter to 3 µm therefore results in a much smaller increase in spread compared to the decrease in spread that results from the same relative increase in fibre diameter

Firstly, as is the case in physiological measurements, Fig. 16a shows that a decrease in the fibre diameter from d_a for both distributed (Dist.) and aligned (Alig.) somas in Fig. 14a and Fig. 15a respectively, to 3 µm in Fig. 14b and Fig. 15b ($\Delta d = 3 - d_a < 0$), results in an increase in the fibre threshold from μ_a in Fig. 14a and Fig. 15a to μ_b in Fig. 14b and Fig. 15b ($\Delta\mu = \mu_b - \mu_a > 0$), and *vice versa*. Compared to the dynamic ranges of the DPFs in Fig. 14 and Fig. 15 (0.3 dB < *DR* < 1.9 dB), the range in threshold change (–1 dB < $\Delta\mu$ < 1 dB) is comparable in magnitude, but not large enough to shift the threshold outside of the original dynamic range. Secondly, although the regression lines of the two cases are almost identical, the distributed case does show more variance relative to its regression line than the aligned case. This suggests that the location of the soma does have an effect on the change in threshold, but less so than does the fibre diameter. Figure 16b shows that a decrease in fibre diameter ($\Delta d < 0$) results in a seemingly inverse exponential increase in DPF spread ($\Delta\sigma > 0$). A decrease in the fibre diameter to 3 µm therefore results in a much smaller increase in spread compared to the decrease in spread that results from the same relative increase in fibre diameter. Compared to Fig. 16a, the distributed case shows much less variance within its distribution, which is now similar to that of the aligned case. This shows that the spread or dynamic range of a single degenerate fibre is primarily determined by the fibre diameter and not affected by the soma location, seeing that the site of excitation is on the axon.

Comparison of the threshold ranges of the different populations (range between the fibres with the highest and lowest stochastic threshold in the population) reveals that fibre diameter has a much smaller impact compared to the location of the soma. A uniform fibre diameter reduces the range from 5 dB for population 1 to 4.3 dB for population 2 (Δ = 0.7 dB) and from 2.6 dB for population 3 to

2.0 dB for population 4 (Δ = 0.6 dB). In contrast, aligning the somas reduces the population threshold range from 5 dB for population 1 to 2.6 dB for population 3 (Δ = 2.4 dB) and from 4.3 dB to 2.0 dB for population 4 (Δ = 2.3 dB). With uniform fibre diameters and aligned somas in population 4, the remaining distribution in thresholds can only be ascribed to the slight variance in soma-electrode distances and the varying fibre-electrode distances because of the 3D distribution of the fibre population within the 5° arc. These observations underline the importance of correctly modelling the location of the electrodes relative to the fibres, and in particular the somatic bundles, to model the threshold range of a population of fibres accurately.

To determine if there is any positive correlation between soma-electrode distance and threshold, Fig. 17 plots the individual fibre thresholds of populations 2 and 4 (all fibres having d_{axon} = 3 µm) versus electrode-soma distance.

It was expected that both populations would show a strong positive correlation, as does the aligned case of population 4. However, the distributed case of population 2 revealed a weak positive correlation with significant variance around its regression line. A possible explanation for the variance of the distributed case might be found by noting from Fig. 5c and Fig. 17 that the soma-electrode distances vary very little on effectively a flat 2D plane for the aligned case whereas the distance varies through a 3D space for the distributed case. The effect of the non-homogenous conductivity of the different materials within the 3D volume conduction model in Fig. 3 might therefore be more pronounced for the 3D distributed case than for the aligned case, which effectively has a near 2D distribution relative to the stimulating electrode.

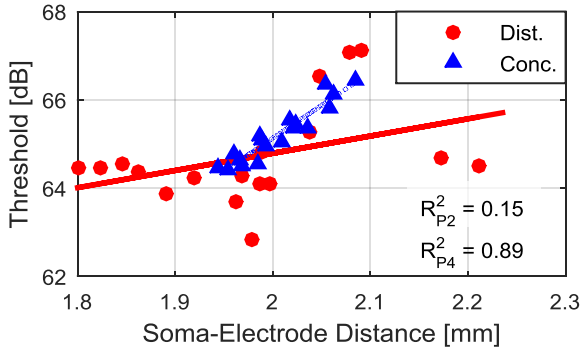

Fig. 17 Fibre thresholds show a strong, positive correlation with the soma-electrode distance for the aligned soma case of population 4, but a weak correlation for the distributed soma case of population 2. This suggests that soma location indeed has a significant impact on the fibre threshold alongside the location of the fibres within the population. A possible explanation for the variance of the distributed case might be that the effect of the non-homogenous conductivity of the different materials within the 3D volume conduction model in Fig. 3 is more pronounced for the 3D distributed case compared to the aligned case, which effectively has a 2D distribution relative to the electrode

Finally, comparing the population thresholds (μ of the thick, dashed DPFs) to the single stochastic and deterministic fibre thresholds (solid lines) reveals a difference of less than 1.0 dB for the distributed somas in Fig. 14 and less than 0.3 dB for the aligned somas in Fig. 15. This suggests that if the objective is to model excitation thresholds, one can safely use the deterministic ANF model to minimise computational effort and time. That being said, the deterministic model cannot account for the dynamic range of a fibre population.

3.4. Pulse train response and temporal analysis

Construction of the temporal plots and histograms was done by stimulating a degenerate stochastic fibre with a pulse-train of 100 pulses at a number of stimulus intensities and extracting from the results the number of propagating APs or spikes, the latency of each AP and the inter-spike intervals. An example of 10 pulses from such a simulation is given in Fig. 18 for a pulse rate of 1000 pps applied to the fibre associated with electrode 11 of user S3R. The excerpt shows the required increase in spikes or APs per second (discharge rate) and decrease in ISI variance with an increase in stimulus intensity (Javel and Shepherd 2000).

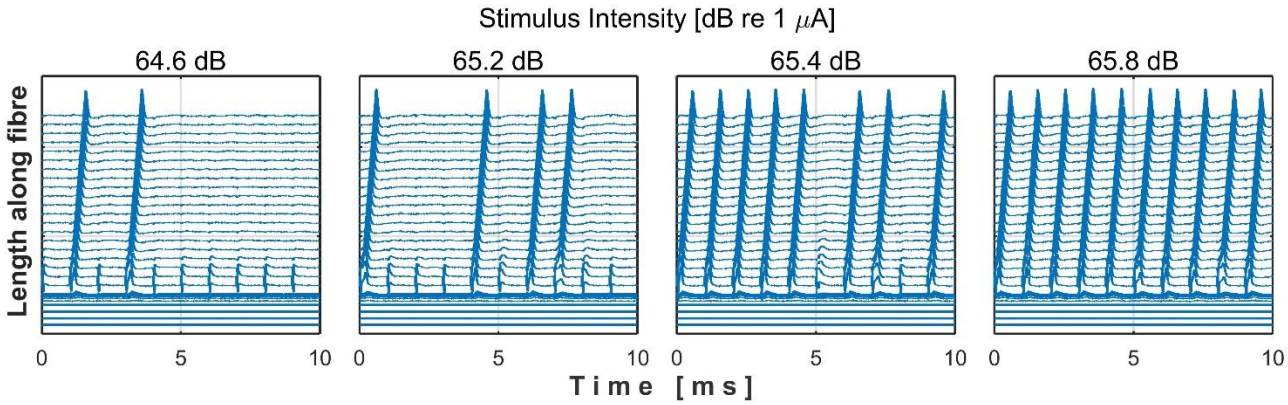

Fig. 18 Propagating APs at increasing stimulus levels at a constant pulse rate of 1000 pps for the degenerate fibre associated with electrode 11 of user S3R having d_{axon} = 3 µm. The figure shows an increase in spikes or APs per second and a decrease in inter-spike intervals (ISIs) variance with an increase in stimulus intensity

From the extracted data the following graphs were generated for user S3R at PWs of 25 µs (Fig. 19a) and 85 µs (Fig. 19b), as well as for user S30R at 25 µs (Fig. 19c) and 85 µs (Fig. 19d): discharge rate, latency and latency standard deviation versus stimulus intensity; period and ISI histograms. The characteristics of these modelled human ANF results could thus be compared and validated against physiological characteristics available for feline ANFs. Because the simulations were done for degenerate fibres, the modelled results are for what is known as a Type A response only, which has a short latency (< 0.44 ms) and a narrow dynamic range (≈ 1.2 dB) because the site of spike initiation is on the central SGC process or axon (Javel and Shepherd 2000).

Discharge Rate

All discharge rate functions show good least squares normal cumulative distribution function fits as is the case for physiological results (Javel and Shepherd 2000; Shepherd and Javel 1997). The dynamic ranges (shown in the legends) are of the correct order of magnitude (Javel and Shepherd 2000) and increase for an increase in pulse rate (Galvin and Fu 2005). For both users the longer PW results in lower threshold stimulus levels whilst S30R, who has scala tympani insertion, has lower threshold stimulus levels compared to S3R, having a scala vestibuli insertion, for both the short and longer PWs due to the scala tympani insertion being closer to the axon on which the AP is initiated.

Latency

The latency plots show the required moderate reduction in latency with increasing stimulus intensity and is of the same order of magnitude as physiological results (Javel and Shepherd 2000; Shepherd and Javel 1997). The same holds true for the latency standard deviations.

Period and ISI Histograms

The period histograms confirm: i) the required short latency, ii) that the response is phase locked to the stimulus pulse shown and iii) that the response becomes more synchronized and greater as in intensity increases (Javel 1990; Javel and Shepherd 2000). The ISI histograms verify: i) that the ISIs have modes at integer multiples of the stimulus period (T) as expected since the response is phase locked, and ii) that the ISI distributions are exponentially decreasing functions of ISI length for submaximal response (Javel 1990). Submaximal response is a response where the spikes per second are fewer than the pulses per second (Javel 1990).

Fig. 19 Temporal analysis of degenerate fibres for users S3R at PW = 25 μs in (a) and PW = 85 μs in (b), as well as user S30R at PW = 25 μs in (c) and PW = 85 μs in (d). The cathodic first, bi-phasic stimuli are shown vs time in the top period histogram in the centre column of each plot. Discharge rate vs stimulus intensity distributions at a number of pulse rates, with corresponding parenthesised mean and dynamic range values, show normal distributions having physiological dynamic ranges that increase for an increase in stimulus intensity. Latency and latency standard deviation vs stimulus intensity distributions have physiological magnitudes that decrease moderately for increasing stimulus intensity as required. Period histograms at 800 pps show phase-locked responses, which increase and become more synchronised with increasing stimulus intensity. ISIs (right-hand column) are seen to be integer multiples of the stimulus period, of which the duration decreases exponentially for submaximal response

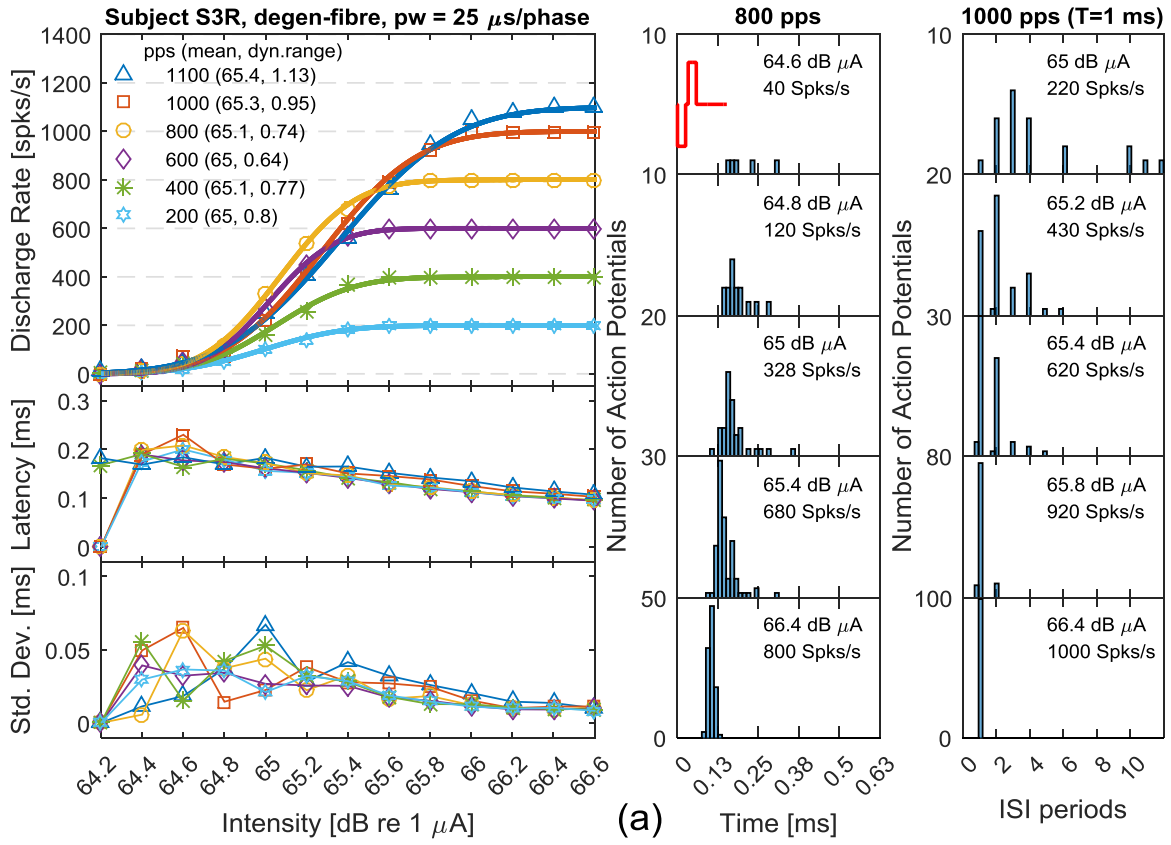
Subject S3R, degen-fibre, pw = 25 μs/phase
pps (mean, dyn.range)
1100 (65.4, 1.13)
1000 (65.3, 0.95)
800 (65.1, 0.74)
600 (65, 0.64)
400 (65.1, 0.77)
200 (65, 0.8)
Discharge Rate [spks/s]
Latency [ms]
Std. Dev. [ms]
Intensity [dB re 1 μA]
800 pps
64.6 dB μA
40 Spks/s
64.8 dB μA
120 Spks/s
65 dB μA
328 Spks/s
65.4 dB μA
680 Spks/s
66.4 dB μA
800 Spks/s
Number of Action Potentials
Time [ms]
1000 pps (T=1 ms)
65 dB μA
220 Spks/s
65.2 dB μA
430 Spks/s
65.4 dB μA
620 Spks/s
65.8 dB μA
920 Spks/s
66.4 dB μA
1000 Spks/s
ISI periods

(a)

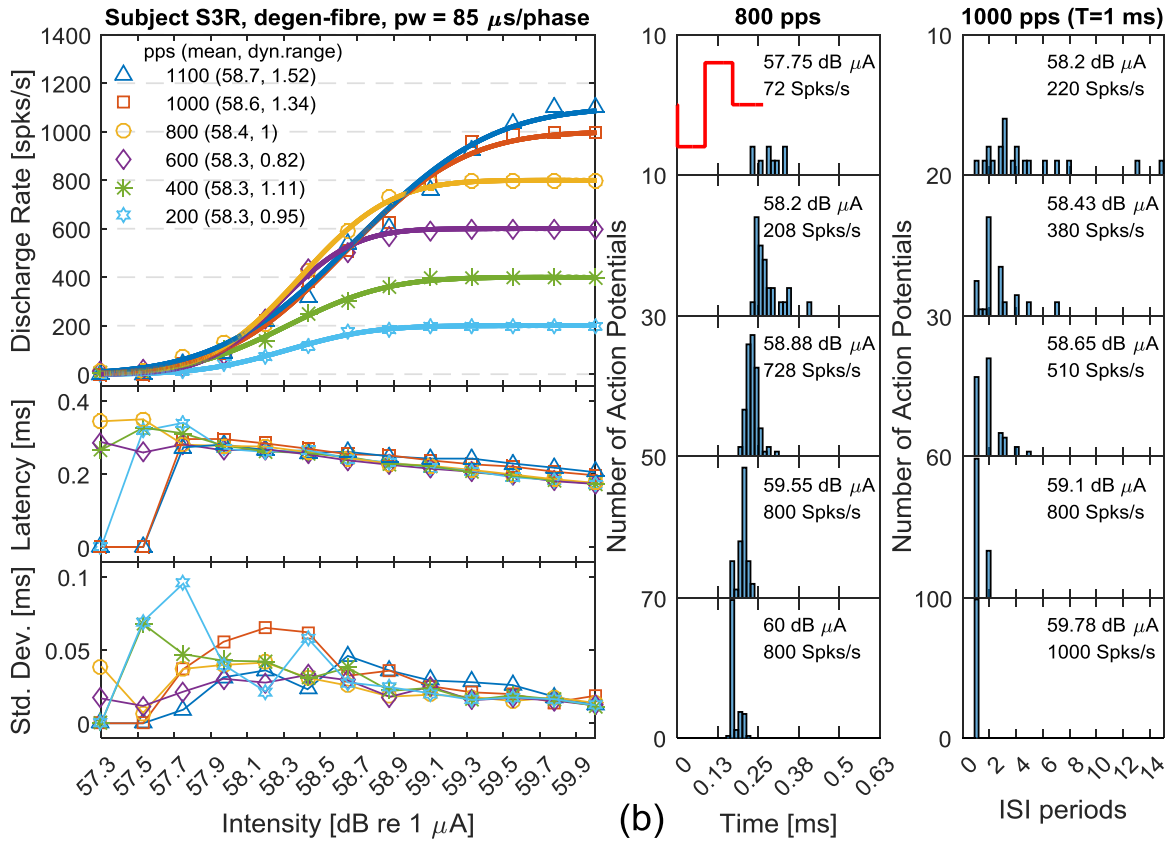
Subject S3R, degen-fibre, pw = 85 μs/phase
pps (mean, dyn.range)
1100 (58.7, 1.52)
1000 (58.6, 1.34)
800 (58.4, 1)
600 (58.3, 0.82)
400 (58.3, 1.11)
200 (58.3, 0.95)
Discharge Rate [spks/s]
Latency [ms]
Std. Dev. [ms]
Intensity [dB re 1 μA]
800 pps
57.75 dB μA
72 Spks/s
58.2 dB μA
208 Spks/s
58.88 dB μA
728 Spks/s
59.55 dB μA
800 Spks/s
60 dB μA
800 Spks/s
Number of Action Potentials
Time [ms]
1000 pps (T=1 ms)
58.2 dB μA
220 Spks/s
58.43 dB μA
380 Spks/s
58.65 dB μA
510 Spks/s
59.1 dB μA
800 Spks/s
59.78 dB μA
1000 Spks/s
ISI periods

(b)

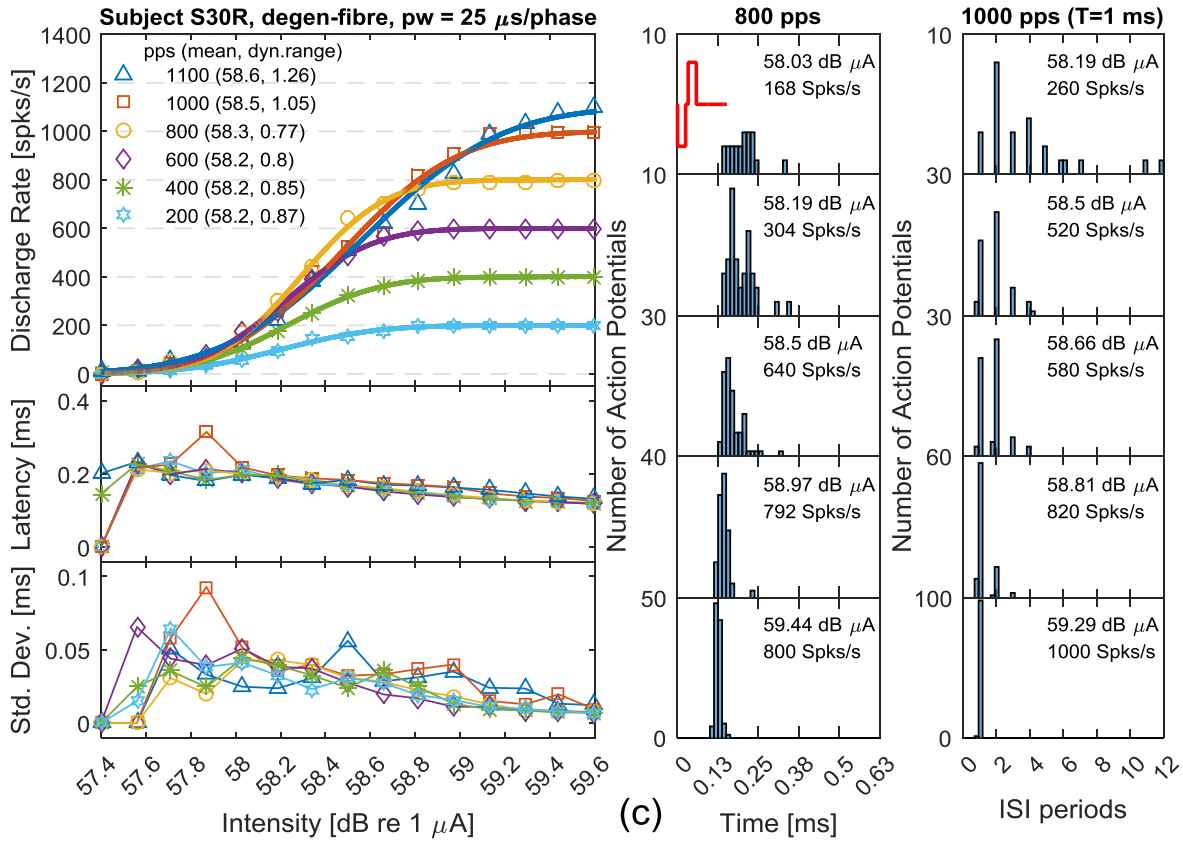
Subject S30R, degen-fibre, pw = 25 μs/phase
pps (mean, dyn.range)
1100 (58.6, 1.26)
1000 (58.5, 1.05)
800 (58.3, 0.77)
600 (58.2, 0.8)
400 (58.2, 0.85)
200 (58.2, 0.87)
Discharge Rate [spks/s]
Latency [ms]
Std. Dev. [ms]
Intensity [dB re 1 μA]
800 pps
58.03 dB μA
168 Spks/s
58.19 dB μA
304 Spks/s
58.5 dB μA
640 Spks/s
58.97 dB μA
792 Spks/s
59.44 dB μA
800 Spks/s
Number of Action Potentials
Time [ms]
1000 pps (T=1 ms)
58.19 dB μA
260 Spks/s
58.5 dB μA
520 Spks/s
58.66 dB μA
580 Spks/s
58.81 dB μA
820 Spks/s
59.29 dB μA
1000 Spks/s
ISI periods
(c)

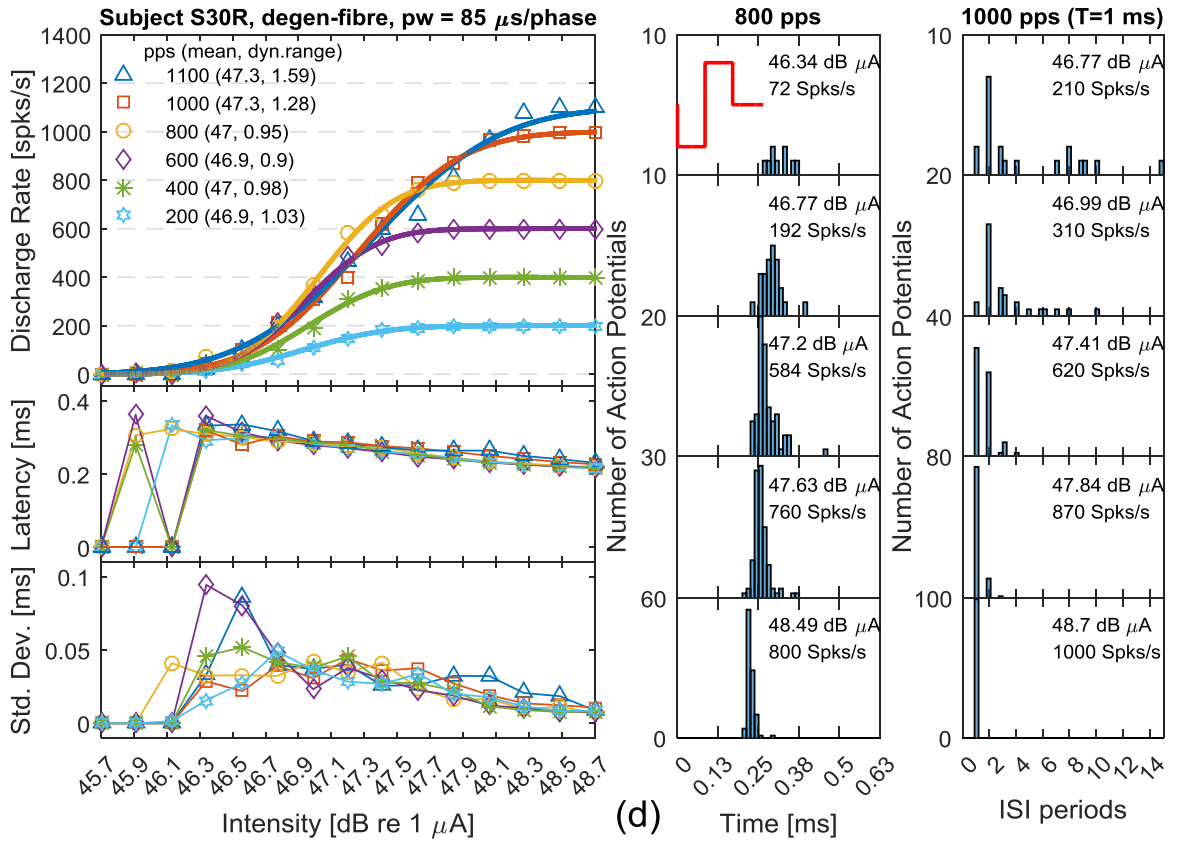
Subject S30R, degen-fibre, pw = 85 μs/phase
pps (mean, dyn.range)
1100 (47.3, 1.59)
1000 (47.3, 1.28)
800 (47, 0.95)
600 (46.9, 0.9)
400 (47, 0.98)
200 (46.9, 1.03)
Discharge Rate [spks/s]
Latency [ms]
Std. Dev. [ms]
Intensity [dB re 1 μA]
800 pps
46.34 dB μA
72 Spks/s
46.77 dB μA
192 Spks/s
47.2 dB μA
584 Spks/s
47.63 dB μA
760 Spks/s
48.49 dB μA
800 Spks/s
Number of Action Potentials
Time [ms]
1000 pps (T=1 ms)
46.77 dB μA
210 Spks/s
46.99 dB μA
310 Spks/s
47.41 dB μA
620 Spks/s
47.84 dB μA
870 Spks/s
48.7 dB μA
1000 Spks/s
ISI periods
(d)

4. Discussion and Conclusions

A purely conductance-based current noise algorithm (Badenhorst et al. 2016) was applied to an HH-based ANF model in VC models of user-specific cochleae, to determine if the excitation threshold and dynamic range of single deterministic and stochastic fibre models are significantly affected by the application of a biophysical stochastic population ANF model. The results in Fig. 10 and Fig. 11 showed adherence to a number of physiological stochastic fibre characteristics: (i) normal DPF distributions (Verveen and Derksen 1968), (ii) negative linear log(*RS*) vs log(diameter) distributions (Rubinstein 1995; Verveen 1962) and (iii) an exponential V_{rms} vs V_{mem} distribution (Verveen 1962).

An intra- and inter-user comparison of stochastic vs deterministic and full vs degenerate fibres for a short and long pulse width in Fig. 12 showed: (i) very little difference in deterministic and stochastic thresholds and narrow dynamic ranges as measured by Javel and Shepherd (2000), (ii) variance in thresholds between users due to a variance in fibre-to-electrode distances as found in Javel et al. (1987), (iii) a decrease in threshold for an increase in pulse width (Javel et al. 1987; Shepherd and Javel 1999) and (iv) a higher threshold for degenerate fibres as the fibre-to-electrode distance increased and the point of excitation moved from the dendrite to the axon. A deadband region was also observed within the deterministic full fibre compound model as shown in Fig. 13, but the cause of this supposed model artifact was deferred for future study.

In an attempt to investigate the stochastic vs deterministic threshold and spread using other ANF models, the well-known Schwarz and Eikhof (1987) (SE) based, humanised gSEF (hgSEF) model (Kalkman et al. 2014) was also implemented using the current noise method and developed numerical SDE solver summarised in par. 2.3. It was however found that the hgSEF model could not converge for time steps larger than 1 ns, which resulted in high memory demand within MATLAB and extremely long computational times relative to the HH-based Rattay model. The reason for requiring such a small step-size was revealed by the authors of the gSEF paper (Briaire and Frijns 2005; Frijns et al. 1995) who stated that their SE-based models were solved using a fourth-order Runge-Kutta algorithm with adaptive step-size control in which the step-size varied between 1 ns and 1 μs. The hgSEF model was therefore not used in the conductance-based stochastic compound ANF model because of its high computational cost resulting from the stiffness of the underlying SE system of differential equations.

Substitution of a single ANF with populations of ANFs having distributed (Fig. 14) and aligned somas (Fig. 15) with varying and uniform diameters first revealed that varying the fibre diameter: (i) has very little effect on the thresholds (Fig. 16a), which are primarily determined by the fibre and soma location relative to the stimulating electrode (Fig. 17) (Javel et al. 1987), (ii) primarily affects the spread or dynamic range of the individual fibres (Fig. 16b) and (iii) has a small impact on the population's threshold range ($\Delta < 0.7$ dB) and the 50% population spread and threshold. In view of the fibre diameter's impact on dynamic range (Fig. 16b) and the smaller range and diameter of human ANFs found in a more recent study by Rattay et al. (2013) (1.7 μm < d_{axon} < 3.5 μm, $d_{axon} = 2.65 \pm 0.3$ μm) and that 71% of axon diameters of adults with sensory neural deafness have been found to be less than 2 μm (42% < 0.5 μm) (Spoendlin and Schrott 1989), future studies should focus on fibres with smaller diameters. Secondly, aligning the somas in Fig. 15 revealed a more significant decrease in the populations' threshold range ($\Delta \approx 2.4$ dB) irrespective of fibre diameter and brought the 50% population threshold even closer to that of the single deterministic and stochastic fibres ($\Delta < 1.0$ dB). These observations highlight the importance of the location of the somas, and hence active fibre compartments, relative to the electrodes within the VC

model. More important however is that a single deterministic fibre fairly accurately provides the activation threshold of the population of fibres it represents, as also found by Kalkman et al. (2015) who implemented a population of deterministic fibres. Adding stochasticity therefore does not solve the persisting problem of compound ANF models greatly overestimating the modelled excitation thresholds (Kalkman et al. 2016).

Pulse train response and temporal analysis of the model in Fig. 19 showed: (i) normal discharge rate vs stimulus intensity distributions having physiological dynamic ranges (Javel and Shepherd 2000; Shepherd and Javel 1997) and (ii) an increase in dynamic range for an increase in pulse rate (Galvin and Fu 2005). Stimulating pulse rates in these simulations were limited to 1100 pps based on user MAP settings, preferences and experimental rates (Arora et al. 2009; Fu and Shannon 2000; Vandali et al. 2000; Xu et al. 1997) in contrast to the high stimulation rates applied in the hybrid model by van Gendt et al. (2016). Studies have also shown that stimulating at higher pulse rates to better utilise CI speech processing schemes through improved temporal information encoding seem to cause negative effects such as poorer modulation detection thresholds (Galvin and Fu 2005), poorer intensity resolution (Kreft et al. 2004) and increased channel interaction (Middlebrooks 2004).

Further evaluation of the temporal results in Fig. 19 showed: (iii) latency and latency standard deviation having physiological magnitudes that decrease moderately for increasing stimulus intensity (Javel and Shepherd 2000; Shepherd and Javel 1997), (iv) phase-locked response which increases and becomes more synchronised with increasing stimulus intensity (period histograms) and (v) ISIs having modes at integer multiples of the stimulus period of which the length decreases exponentially for submaximal response (Javel 1990; Javel and Shepherd 2000). As the order of magnitude of the dynamic range of the discharge rate curves as well as the latencies are being compared to those of felines, one should consider that feline ANFs have much smaller diameters, that the dendrite is significantly shorter and that the soma is myelinated. The larger human diameters will therefore result in lower thresholds and smaller dynamic ranges as seen from Fig. 16b, as well as shorter latencies if the point of excitation is on the axon as in the case of these degenerate models. In the case of full fibres, the point of excitation will most likely be on the dendrite, in which case the longer dendrite and unmyelinated human soma will cause a delay in the propagating AP, thereby increasing the latency (Rattay et al. 2001b). An important temporal characteristic not yet included in the presented model is that of adaptation, as it has been shown that low-threshold potassium (KLT) and hyperpolarisation-activated cation (HCN) channels need to be included in the HH model. This has however only been done on a single node of Ranvier (Negm and Bruce 2014). It has also been observed in felines and rats that adaptation is more prevalent at relatively high pulse rates (> 1000 pps) (Haenggeli et al. 1998; Litvak et al. 2001; Miller et al. 2008), whereas the users modelled in this study have relatively low pulse rates of between 500 pps and 900 pps (Table 1).

In conclusion, the study has shown that the purely conductance-based stochastic nerve fibre model could successfully be implemented in user-specific compound ANF models and sufficiently model stochastic and temporal characteristics for application in future studies. Although neither the stochastic nor the population models improved the modelling of the deterministic thresholds, they did provide a means to model and evaluate dynamic range and some temporal characteristics. Simulation of the dynamic range could possibly be compared to clinical measurements of users' dynamic range. The stochastic population model is currently being evaluated in the modelling of electrically evoked compound action potentials (eCAPs) as a means of validating the compound model using measured eCAPs and to investigate the possibility of using eCAPs to determine sites of neural degeneration. Future temporal evaluation of

the proposed stochastic model could be done by including the ionic channels required for adaptation in a single fibre and comparing the temporal and computational performance to channel-based stochastic models (Goldwyn et al. 2011). Computational performance is however of great importance if these models are to be applied in clinical evaluations and investigations. The proposed model could also be used to model user-specific temporally encoded information, which influences the speech perception of CI users. Being able to model the above temporal characteristics is a significant step towards closing the gap between modelling the ESNR and comparing it to psychoacoustic experiments so as to improve understanding of the wide variance in user speech perception of CI users. Combined with user-specific VC models, improved modelling of the ESNR will also allow for improved modelling of stimulation strategies and CI electrode designs, which will in turn allow for improving the sound and speech perception of the CI user.

References

Agterberg MJH, Versnel H, de Groot JCMJ, van den Broek M, Klis SFL (2010) Chronic electrical stimulation does not prevent spiral ganglion cell degeneration in deafened guinea pigs. Hearing Research 269:169-179

Arora K, Dawson P, Dowell R, Vandali A (2009) Electrical stimulation rate effects on speech perception in cochlear implants. Int J Audiol 48:561-567

Badenhorst W, Hanekom T, Hanekom JJ (2016) Development of a voltage dependent current noise algorithm for conductance based stochastic modelling of auditory nerve fibres. Biological Cybernetics 110:403-416 doi:10.1007/s00422-016-0694-6

Briaire JJ, Frijns JHM (2005) Unraveling the electrically evoked compound action potential. Hearing Research 205:143-156 doi:10.1016/j.heares.2005.03.020

Briaire JJ, Frijns JHM (2006) The consequences of neural degeneration regarding optimal cochlear implant position in scala tympani: A model approach. Hearing Research 214:17-27 doi:10.1016/j.heares.2006.01.015

Bruce IC, Irlicht LS, White MW, O'Leary SJ, Dynes S, Javel E, Clark GM (1999a) A stochastic model of the electrically stimulated auditory nerve: pulse-train response. Biomedical Engineering, IEEE Transactions on 46:630-637 doi:10.1109/10.764939

Bruce IC, White MW, Irlicht LS, O'Leary SJ, Dynes S, Javel E, Clark GM (1999b) A stochastic model of the electrically stimulated auditory nerve: single-pulse response. Biomedical Engineering, IEEE Transactions on 46:617-629 doi:10.1109/10.764938

Cartee LA, van den Honert C, Finley CC, Miller RL (2000) Evaluation of a model of the cochlear neural membrane. I. Physiological measurement of membrane characteristics in response to intrameatal electrical stimulation. Hearing Research 146:143-152 doi:10.1016/S0378-5955(00)00109-X

Coco A, Epp SB, Fallon JB, Xu J, Millard RE, Shepherd RK (2007) Does cochlear implantation and electrical stimulation affect residual hair cells and spiral ganglion neurons? Hearing Research 225:60-70

Dangerfield CE, Kay D, Burrage K (2010) Stochastic models and simulation of ion channel dynamics. Procedia Computer Science 1:1587-1596 doi:0.1016/j.procs.2010.04.178

Du Q, Faber V, Gunzburger M (1999) Centroidal Voronoi Tessellations: Applications and Algorithms. SIAM Review 41:637-676 doi:10.1137/S0036144599352836

Felder E, Kanonier G, Scholtz A, Rask-Andersen H, A Schrott-Fischer A (1997) Quantitative evaluation of cochlear neuronal and computer-aided three-dimensional reconstruction of spiral ganglion cells in humans with a peripheral loss of nerve fibres. Hearing Research 105:183-190

Ferguson WD, Collins LM, Smith DW (2003) Psychophysical threshold variability in cochlear implant subjects. Hearing Research 180:101-113 doi:10.1016/s0378-5955(03)00111-4

Firszt JB et al. (2004) Recognition of speech presented at soft to loud levels by adult cochlear implant recipients of three cochlear implant systems. Ear and Hearing 25:375-387

Frijns JHM, de Snoo SL, Schoonhoven R (1995) Potential distributions and neural excitation patterns in a rotationally symmetric model of the electrically stimulated cochlea. Hearing Research 87:170-186 doi:10.1016/0378-5955(95)00090-q

Frijns JHM, Mooij J, ten Kate JH (1994) A quantitative approach to modeling mammalia myelinated nerve fibers for electrical prostheis design. IEEE Transaction on Biomedical Engineering 41:556-566

Fu Q-J, Shannon RV (2000) Effect of stimulation rate on phoneme recognition by Nucleus-22 cochlear implant listeners. The Journal of the Acoustical Society of America 107:589-597 doi:10.1121/1.428325

Galvin JJ, Fu Q-J (2005) Effects of Stimulation Rate, Mode and Level on Modulation Detection by Cochlear Implant Users. Journal of the Association for Research in Otolaryngology 6:269-279 doi:10.1007/s10162-005-0007-6

Goldwyn JH, Imennov NS, Famulare M, Shea-Brown E (2011) Stochastic differential equation models for ion channel noise in Hodgkin-Huxley neurons. Physical Review E - Statistical, Nonlinear, and Soft Matter Physics 83:041908 doi:10.1103/PhysRevE.83.041908

Goldwyn JH, Shea-Brown E (2011) The what and where of adding channel noise to the Hodgkin-Huxley equations. PLoS computational biology 7:e1002247 doi:10.1371/journal.pcbi.1002247

Govender N (2006) A brief analysis of certain numerical methods used to solve stochastic differential equations. University of Pretoria

Haenggeli A, Zhang JS, Fischer MW, Pelizzone M, Rouiller EM (1998) Electrically Evoked Compound Action Potential (ECAP) of the Cochlear Nerve in Response to Pulsatile Electrical Stimulation of the Cochlea in the Rat: Effects of Stimulation at High Rates. Audiology 37:353-371 doi:10.3109/00206099809072989

Hales JP, Lin CSY, Bostock H (2004) Variations in excitability of single human motor axons, related to stochastic properties of nodal sodium channels. Journal of Physiology 559:953-964

Hanekom T (2001) Three-dimensional spiraling finite element model of the electrically stimulated cochlea. Ear and Hearing 22:300-315

Hanekom T, Hanekom JJ (2016) Three-dimensional models of cochlear implants: A review of their development and how they could support management and maintenance of cochlear implant performance. Network: Computation in Neural Systems:1-40 doi:10.3109/0954898X.2016.1171411

Higham DJ (2001) An Algorithmic Introduction to Numerical Simulation of Stochastic Differential Equations. SIAM Review 43:525-546 doi:doi:10.1137/S0036144500378302

Hodgkin AL, Huxley AF (1952) A quantitative description of membrane current and its application to conduction and excitation in nerve. Journal of Physiology 117:500-544

Huang Y, Rüdiger S, Shuai J (2013) Langevin approach for stochastic Hodgkin–Huxley dynamics with discretization of channel open fraction. Physics Letters A 377:3223-3227 doi:10.1016/j.physleta.2013.10.008

Imennov NS, Rubinstein JT (2009) Stochastic Population Model for Electrical Stimulation of the Auditory Nerve. IEEE Transactions on Biomedical Engineering 56:2493-2501 doi:10.1109/TBME.2009.2016667

Izhikevich EM (2004) Which model to use for cortical spiking neurons? Neural Networks, IEEE Transactions on 15:1063-1070 doi:10.1109/tnn.2004.832719

Javel E (1990) Acoustic and Electrical Encoding of Temporal Information. In: Miller JM, Spelman FA (eds) Cochlear Implants - Models of the Electrically Stimulated Ear. Springer-Verlag, New York, pp 247-295

Javel E, Shepherd RK (2000) Electrical stimulation of the auditory nerve: III. Response initiation sites and temporal fine structure. Hearing Research 140:45-76 doi:10.1016/s0378-5955(99)00186-0

Javel E, Tong YC, Shepherd RK, Clark GM (1987) Responses of cat auditory nerve fibers to biphasic electrical current pulses. Annals of Otology, Rhinology & Laryngology 96:26-30

Kalkman RK, Briaire JJ, Dekker DM, Frijns JH (2014) Place pitch versus electrode location in a realistic computational model of the implanted human cochlea. Hearing Research 315C:10-24 doi:10.1016/j.heares.2014.06.003

Kalkman RK, Briaire JJ, Frijns JHM (2015) Current focussing in cochlear implants: An analysis of neural recruitment in a computational model. Hearing Research 322:89-98 doi:10.1016/j.heares.2014.12.004

Kalkman RK, Briaire JJ, Frijns JHM (2016) Stimulation strategies and electrode design in computational models of the electrically stimulated cochlea: An overview of existing literature. Network: Computation in Neural Systems:1-28 doi:10.3109/0954898X.2016.1171412

Kreft HA, Donaldson GS, Nelson DA (2004) Effects of pulse rate and electrode array design on intensity discrimination in cochlear implant users. The Journal of the Acoustical Society of America 116:2258-2268 doi:10.1121/1.1786871

Kwon BJ, Van Den Honert C (2006) Effect of electrode configuration on psychophysical forward masking in cochlear implant listeners. Journal of the Acoustical Society of America 119:2994-3002

Litvak L, Delgutte B, Eddington D (2001) Auditory nerve fiber responses to electric stimulation: Modulated and unmodulated pulse trains. Journal of the Acoustical Society of America 110:368-379 doi:10.1121/1.1375140

Lu CB, Schuknecht HF (1994) Pathology of prelingual profound deafness: Magnitude of labyrinthitis fibro-ossificans. American Journal of Otology 15:74-85

Macherey O, Carlyon RP, Van Wieringen A, Wouters J (2007) A dual-process integrator-resonator model of the electrically stimulated human auditory nerve. Journal of the Association for Research in Otolaryngology 8:84-104

Malherbe TK (2009) Development of a method to create subject specific cochlear models for electric hearing. University of Pretoria
Malherbe TK, Hanekom T, Hanekom JJ (2013) Can subject-specific single-fibre electrically evoked auditory brainstem response data be predicted from a model? Medical Engineering & Physics 35:926-936 doi:10.1016/j.medengphy.2012.09.001
Malherbe TK, Hanekom T, Hanekom JJ (2015) The effect of the resistive properties of bone on neural excitation and electric fields in cochlear implant models. Hearing Research 327:126-135 doi:10.1016/j.heares.2015.06.003
Middlebrooks JC (2004) Effects of cochlear-implant pulse rate and inter-channel timing on channel interactions and thresholds. The Journal of the Acoustical Society of America 116:452-468 doi:10.1121/1.1760795
Miller CA, Hu N, Zhang F, Robinson BK, Abbas PJ (2008) Changes across time in the temporal responses of auditory nerve fibers stimulated by electric pulse trains. JARO - Journal of the Association for Research in Otolaryngology 9:122-137 doi:10.1007/s10162-007-0108-5
Nadol JB, Young YS, Glynn RJ (1989) Survival of spiral ganglion cells in profound sensorineural hearing loss: Implications for cochlear implantation. Annals of Otology, Rhinology & Laryngology 98:411-416 doi:10.1177/000348948909800602
Nadol Jr JB (1990) Degeneration of cochlear neurons as seen in the spiral ganglion of man. Hearing Research 49:141-154 doi:10.1016/0378-5955(90)90101-t
Nadol Jr JB (1997) Patterns of neural degeneration in the human cochlea and auditory nerve: Implications for cochlear implantation. Otolaryngology - Head and Neck Surgery 117:220-228 doi:10.1016/s0194-5998(97)70178-5
Negm MH, Bruce IC (2014) The Effects of HCN and KLT Ion Channels on Adaptation and Refractoriness in a Stochastic Auditory Nerve Model. IEEE Transactions on Biomedical Engineering 61:2749-2759 doi:10.1109/TBME.2014.2327055
O'Brien GE (2016) Biophysical Population Models of the Auditory Nerve. University of Washington
O'Brien GE, Rubinstein JT (2016) The development of biophysical models of the electrically stimulated auditory nerve: Single-node and cable models. Network: Computation in Neural Systems 27:135-156 doi:10.3109/0954898x.2016.1162338
Otte J, Schuknecht HF, Kerr AG (1978) Ganglion cell populations in normal and pathological human cochleae implications for cochlear implantation. Laryngoscope 88:1231-1246
Rattay F (1987) Ways to approximate current-distance relations for electrically stimulated fibers. Journal of Theoretical Biology 125:339-349 doi:10.1016/s0022-5193(87)80066-8
Rattay F (1990) Electrical Nerve Stimulation, Theory, Experiments and Applications. 1 edn. Springer, Vienna
Rattay F, Leao RN, Felix H (2001a) A model of the electrically excited human cochlear neuron. II. Influence of the three-dimensional cochlear structure on neural excitability. Hearing Research 153:64-79 doi:10.1016/s0378-5955(00)00257-4
Rattay F, Lutter P, Felix H (2001b) A model of the electrically excited human cochlear neuron: I. Contribution of neural substructures to the generation and propagation of spikes. Hearing Research 153:43-63 doi:10.1016/s0378-5955(00)00256-2
Rattay F, Potrusil T, Wenger C, Wise AK, Glueckert R, Schrott-Fischer A (2013) Impact of Morphometry, Myelinization and Synaptic Current Strength on Spike Conduction in Human and Cat Spiral Ganglion Neurons. PLoS ONE 8:e79256 doi:10.1371/journal.pone.0079256
Rubinstein JT (1995) Threshold fluctuations in an N sodium channel model of the node of Ranvier. Biophysical journal 68:779-785
Sachs MB, Voigt HF, Young ED (1983) Auditory nerve representation of vowels in background noise. Journal of Neurophysiology 50:27-45
Schwarz JR, Eikhof G (1987) Na current and action potentials in rat myelinated nerve fibres at 20 and 37°C. European Journal of Physiology 409:569-577
Shepherd RK, Javel E (1997) Electrical stimulation of the auditory nerve. I. Correlation of physiological responses with cochlear status. Hearing Research 108:112-144 doi:10.1016/s0378-5955(97)00046-4
Shepherd RK, Javel E (1999) Electrical stimulation of the auditory nerve: II. Effect of stimulus waveshape on single fibre response properties. Hearing Research 130:171-188 doi:10.1016/s0378-5955(99)00011-8

Sigworth FJ (1980) The variance of sodium current fluctuations at the node of Ranvier. Journal of Physiology 307:97-129
Skinner MW (2003) Optimizing cochlear implant speech performance. The Annals of otology, rhinology & laryngology Supplement 191:4-13
Smit JE, Hanekom T, Hanekom JJ (2009) Estimation of stimulus attenuation in cochlear implants. Journal of Neuroscience Methods 180:363-373
Smit JE, Hanekom T, van Wieringen A, Wouters J, Hanekom JJ (2010) Threshold predictions of different pulse shapes using a human auditory nerve fibre model containing persistent sodium and slow potassium currents. Hearing Research 269:12-22 doi:10.1016/j.heares.2010.08.004
Snel-Bongers J, Briaire JJ, Vanpoucke FJ, Frijns JHM (2012) Spread of excitation and channel interaction in single-and dual-electrode cochlear implant stimulation. Ear and Hearing 33:367-376
Spoendlin H, Schrott A (1989) Analysis of the human auditory nerve. Hearing Research 43:25-38
van den Honert C, Stypulkowski PH (1987) Temporal response patterns of single auditory nerve fibers elicited by periodic electrical stimuli. Hearing Research 29:207-222
van Gendt MJ, Briaire JJ, Kalkman RK, Frijns JHM (2016) A fast, stochastic, and adaptive model of auditory nerve responses to cochlear implant stimulation. Hearing Research 341:130-143 doi:10.1016/j.heares.2016.08.011
van Gendt MJ, Briaire JJ, Kalkman RK, Frijns JHM (2017) Modeled auditory nerve responses to amplitude modulated cochlear implant stimulation. Hearing Research 351:19-33 doi:http://dx.doi.org/10.1016/j.heares.2017.05.007
Vandali AE, Whitford LA, Plant KL, Clark, M. G (2000) Speech Perception as a Function of Electrical Stimulation Rate: Using the Nucleus 24 Cochlear Implant System. Ear and Hearing 21:608-624
Verveen AA (1962) Axon diameter and fluctuation in excitability. Acta Morphologica Neerlando-Scandinavica 5:79-85
Verveen AA, Derksen HE (1968) Fluctuation phenomena in nerve membrane. Proceedings of the IEEE 56:906-916 doi:10.1109/proc.1968.6443
Xu J, Shepherd RK, Millard RE, Clark GM (1997) Chronic electrical stimulation of the auditory nerve at high stimulus rates: a physiological and histopathological study. Hearing Research 105:1-29 doi:10.1016/S0378-5955(96)00193-1